Polynomial reconstruction of the magnetic field observed by multiple spacecraft with integrated velocity determination

Richard E. Denton[1], Yi-Hsin Liu[1], Hiroshi Hasegawa[2], Roy B. Torbert[3], Wenya Li[4], Stephen Fuselier[5,6], and James L. Burch[5]

[1]Department of Physics and Astronomy, Dartmouth College, Hanover, New Hampshire, USA
[2]Institute of Space and Astronautical Science, JAXA, Sagamihara, Japan
[3]Institute for the Study of Earth, Oceans, and Space, University of New Hampshire, Durham, New Hampshire, USA
[4]State Key Laboratory of Space Weather, National Space Science Center, Chinese Academy of Sciences, Beijing, China
[5]Space Science and Engineering Division Southwest Research Institute, San Antonio, Texas, USA
[6]University of Texas at San Antonio, San Antonio, Texas, USA

Key Points:

- Polynomial reconstruction using multiple input times yields improved reconstructions and an estimate of the structure velocity.
- Using reconstructions of simulation data, the effect of various options is explored and recommendations for method are made.
- Two MMS events are reconstructed, showing that events lacking MMS4 current density and events without an X line are also reconstructed.

Corresponding author: Richard E. Denton, `redenton at gmail dot com`

Abstract

Recently a polynomial reconstruction technique has been developed for reconstructing the magnetic field in the vicinity of multiple spacecraft, and has been applied to events observed by the Magnetospheric Multiscale (MMS) mission. Whereas previously the magnetic field was reconstructed using spacecraft data from a single time, here we extend the method to allow input over a span of time. This extension increases the amount of input data to the model, improving the reconstruction results, and allows the velocity of the magnetic structure to be calculated. The effect of this modification, as well as many other options, is explored by comparing reconstructed fields to those of a three-dimensional particle in cell simulation of magnetic reconnection, using virtual spacecraft data as input. We often find best results using multiple-time input, a moderate amount of smoothing of the input data, and a model with a reduced set of parameters based on the ordering that the maximum, intermediate, and minimum values of the gradient of the vector magnetic field are well separated. When spacecraft input data are temporally smoothed, reconstructions are representative of spatially smoothed fields. Two MMS events are reconstructed. The first of these was late in the mission when it was not possible to use the current density for MMS4 because of its instrument failure. The second shows a rotational discontinuity without an X or O line. In both cases, the reconstructions yield a visual representation of the magnetic structure that is consistent with earlier studies.

Plain Language Summary

The magnetic field plays a crucial role in many space physics processes. Ideally, we would image the magnetic field, but spacecraft make only point observations. Reconstruction techniques allow us to infer the structure of the magnetic field around the trajectory of spacecraft and to visualize that structure. Here we extend our previous technique of polynomial expansion of the magnetic field by using input from spacecraft over a span of time rather than at just one point in time. We test the new technique, as well as our previous technique, by reconstructing the magnetic field around the trajectory of virtual spacecraft flying through a simulation of magnetic reconnection. Then we use our new technique to reconstruct the magnetic field around the trajectory of the Magnetospheric Multiscale (MMS) spacecraft for two events observed in space.

1 Introduction

The magnetic field plays a crucial role in magnetic reconnection and other space physics processes. In order to understand these processes, it is helpful to determine the structure of the magnetic field and the velocity of that structure relative to the spacecraft. Single spacecraft techniques to determine both the structure and velocity include reconstruction based on Grad-Shafranov equilibrium (Sonnerup et al., 2006, and references therein), magnetohydrodynamics (MHD) and Hall MHD (Sonnerup & Teh, 2008, 2009), and electron MHD (EMHD) (Hasegawa et al., 2019; Korovinskiy et al., 2021, and references therein). Empirical models using observations by multiple spacecraft of the magnetic field have also been developed. First order Taylor expansion (FOTE) of the magnetic field has been described by Fu et al. (2015, 2016, 2020). Recently Torbert et al. (2020) and then Denton et al. (2020) extended this technique to a quadratic model using the current density measured by the spacecraft as an input to the model, and applied these techniques to events observed by the Magnetospheric Multiscale (MMS) mission. The empirical methods have fewer assumptions than the single spacecraft techniques and yield time-dependent maps of the magnetic field around the spacecraft.

Using the reconstruction method of Denton et al. (2020), Denton et al. (2021) used the varying location of the reconstructed reconnection X-line relative to the spacecraft to estimate the velocity of the magnetic structure. (The reconnection X-line is the magnetic null of the magnetic field in the plane containing the reconnection magnetic field and direction across the current sheet.) Basically, this technique assumed that the reconnection structure, or at least the position of the X-line, was time stationary or at least slowly varying. In this paper, we will also use polynomial reconstruction to reconstruct the magnetic field and determine the structure velocity, but using a more integrated technique. We will assume that the structure velocity is constant during some segment of time that includes multiple times at which the data was sampled, and will find the velocity and reconstruction parameters that lead to a best fit to all the spacecraft magnetic field and current density observations during that time segment. The resulting velocity optimizes the fit to all the data, not just the position of an inferred X-line. We will call this new method "multiple-time input", as distinguished from the "single-time input" method of Denton et al. (2020).

Here we test the multiple-time input technique using data from a 3D particle-in-cell simulation of magnetic reconnection with small but nontrivial spatial variation out of the reconnection plane (Liu et al., 2019). Then we use this technique to determine the magnetic structure for two events observed by MMS.

In section 2 we briefly discuss the data and method, in section 3 we reconstruct the magnetic field for the simulation data, in section 4 we reconstruct the magnetic field for two MMS events. Finally in section 5 we summarize our results.

The largest section of this paper tests various options for reconstruction in section 3. For someone interested only in actual MMS events, they may want to skim through section 2 and then skip to section 4. Section 3 is important for learning what options work best and how well the reconstructions agree with the actual fields that are being reconstructed, but the results of section 3 are also summarized in section 5.

A new and key feature of our simulation data is that they are three dimensional. As we will see, it is challenging to accurately reconstruct the variation of the fields in the direction of least spatial variation (minimum gradient).

2 Reconstruction method

What we want to do is to get a quadratic expansion of the magnetic field in terms of the reconnection coordinates L, M, and N; L and N define the reconnection plane, where L is aligned with the direction of the reconnection magnetic field and N is the "normal" direction across the current sheet; M completes the coordinate system, and is ideally the direction of invariance, although that may not be the case if the L direction is determined based on maximum variance of $\mathbf{B}$ (Denton et al., 2016, 2018). Note that we use L, M, and N (or l, m, and n discussed below) as either coordinates or component labels, similar to the way x, y, and z are commonly used.

The complete quadratic expansion in terms of these coordinates is

$$\begin{aligned} B_i \quad = \quad & B_{i,0} + \frac{\partial B_i}{\partial L} L + \frac{\partial B_i}{\partial M} M + \frac{\partial B_i}{\partial N} N \\ & + \frac{\partial^2 B_i}{\partial L^2} \frac{L^2}{2} + \frac{\partial^2 B_i}{\partial M^2} \frac{M^2}{2} + \frac{\partial^2 B_i}{\partial N^2} \frac{N^2}{2} \\ & + \frac{\partial^2 B_i}{\partial L \partial M} LM + \frac{\partial^2 B_i}{\partial L \partial N} LN + \frac{\partial^2 B_i}{\partial M \partial N} MN, \end{aligned} \tag{1}$$

where the i subscript in B_i stands for L, M, or N. The equations for $\mu_0 \mathbf{J} = \nabla \times \mathbf{B}$ (neglecting the displacement current) and $\nabla \cdot \mathbf{B} = \mathbf{0}$ are found by taking the curl or divergence of equations (1) as described in Appendix A. We assume that there are four spacecraft. And for each of these spacecraft, there are three components of $\mathbf{B}$ and three components of $\mathbf{J}$, leading to 24 equations. There are also four equations from $\nabla \cdot \mathbf{B} = \mathbf{0}$, one for spatially constant terms, and three derived from terms proportional to L, M, or N (Appendix A). For more details, see work by Denton et al. (2020).

For each of equations (1), with $i = L$, M, or N, there are 10 parameters; so altogether, there are 30 parameters to determine at any one time. Using data from a single time, there are 24 plus 4 equals 28 equations, not enough to solve for all 30 parameters. To get around this problem, Torbert et al. (2020) and Denton et al. (2020) used models depending on the coordinates n, l, and m based on Minimum Directional Derivative (MDD) analysis, which calculates the gradient of the vector magnetic field measured by four spacecraft (Shi et al., 2005, 2019); n, l, and m are the maximum, intermediate, and minimum gradient eigenvector coordinates, respectively. Normally the direction of the maximum gradient will be the direction across the current sheet, $\sim \mathbf{e}_N$ (Denton et al., 2018). Then if the minimum gradient is relatively steady and approximately in the $\mathbf{e}_M$ direction, l, m, and n will be similar to L, M, and N.

Based on the fact that the linear m dependence is by definition smallest, Torbert et al. (2020) dropped the $\partial^2 B_i/\partial m^2$ terms and used a superposition of solutions with 28 parameters in order to exactly match the values of $\mathbf{B}$ and $\mathbf{J}$ at the spacecraft positions. But Denton et al. (2020) showed that that procedure results in overfitting, leading to a solution that could wildly vary away from the spacecraft positions. The problem is similar to that resulting from use of a high order polynomial with respect to one variable to exactly fit a number of data points. In order to avoid overfitting, Denton et al. (2020) used a reduced set of terms based on the ordering $\partial/\partial n \gg \partial/\partial l \gg \partial/\partial m$.

Now we introduce our multiple-time input approach using measurements over an interval of time. We will assume that the spacecraft are moving through the magnetic structure with a constant velocity for several observation times. This is similar in principle to the method of Manuzzo et al. (2019), who used several data points to evaluate the structure velocity from the potentially single-point Spatial-Temporal Difference (STD) method of Shi et al. (2006). STD as implemented by Shi et al. (2006) assumes that the time dependence of the magnetic field observed by all four spacecraft is due to convection through a steady spatial structure, and solves for the structure velocity from the convection equation using the spatial gradient of the magnetic field evaluated at one time. Most other systems of reconstruction also assume a constant velocity over a period of time (e.g. Hasegawa et al., 2019).

Expanding L, M, and N, or l, m, and n around the centroid of the spacecraft at the central time of the time segment, we can use the constant velocity to calculate the coordinates of the spacecraft at earlier or later times. Then we can get a best fit to all the data, 24 equations for each observation time plus the four $\nabla \cdot \mathbf{B} = \mathbf{0}$ conditions. In practice, we start with a guess for the velocity using the STD method, and then use a nonlinear minimization routine (Matlab fminsearch) to find the velocity that minimizes the squared difference between the model and the observations.

Like Denton et al. (2020), we normalize distances to the average spacecraft spacing d_{sc}. Then $\mathbf{B}$ and $\mu_0 \mathbf{J} = \nabla \times \mathbf{B}$ have the same units for the least-squares calculation. We also satisfy $\nabla \cdot \mathbf{B} = \mathbf{0}$ exactly. Using the complete quadratic expansion in equations (1), there is no need to rotate to the MDD coordinates, as was done by Torbert et al. (2020) and Denton et al. (2020, 2021). However, we also consider solutions using reduced sets of equations with fewer terms (Denton et al., 2020). In that case, we normally evaluate the solution for each data time segment (set of observation times) in the MDD l-m-n frame of the central time value of that time segment. Then the resulting reconstructed fields are rotated back to the L-M-N coordinate system for comparison to the simulation or MMS data.

Denton et al. (2020) called a model that neglected $\partial^2 B_i/\partial m^2$ terms, but kept all the other terms in the quadratic expansion, "full quadratic", and abbreviated the name of the model as Q-3D. This model has the same equations as equations (1) neglecting the $\partial^2 B_i/\partial M^2$ terms, but with M, L, and N replaced by m, l, and n, respectively. To avoid confusion with our past nomenclature, we will abbreviate the name of the "com-

Table 1. Characteristics of reconstruction models

Model	Abreviation	Uses $\mathbf{J}$ as input	$\partial^2/\partial m^2$	$\partial^2/\partial m\partial n$ $\partial^2/\partial m\partial l$	$\partial/\partial m$	$\partial^2 B_n/\partial n^2$ $\partial^2 B_l/\partial l^2$ $\partial^2 B_n/\partial n\partial l$ $\partial^2 B_l/\partial n\partial l$
3D Complete Quadratic	CQ-3D	Yes	Yes	Yes	Yes	Yes
3D Quadratic	Q-3D	Yes	No	Yes	Yes	Yes
3D Reduced Quadratic	RQ-3D	Yes	No	No	Yes	No
3D Linear with only $\mathbf{B}$ as input	LB-3D	No	No	No	Yes	No
2D models	-2D	Depends[a]	No	No	No	Depends[a]

[a]Depends on the particular model.

plete quadratic" model in equations (1) as CQ-3D, and maintain the same model abbreviations for the "full quadratic", "reduced quadratic", and linear models as were used by Denton et al. (2020), Q-3D, RQ-3D, and LB-3D respectively. In terms of the local MDD ccordinates, m, l, and n, the equations of the 3D reduced quadratic (RQ-3D) are

$$\begin{aligned} B_l &= B_{l,0} + \frac{\partial B_l}{\partial n} n + \frac{\partial B_l}{\partial l} l + \frac{\partial B_l}{\partial m} m + \frac{\partial^2 B_l}{\partial n^2}\frac{n^2}{2} && (2) \\ B_m &= B_{m,0} + \frac{\partial B_m}{\partial n} n + \frac{\partial B_m}{\partial l} l + \frac{\partial B_m}{\partial m} m && (3) \\ &\quad + \frac{\partial^2 B_m}{\partial n^2}\frac{n^2}{2} + \frac{\partial^2 B_m}{\partial n \partial l} nl + \frac{\partial^2 B_m}{\partial l^2}\frac{l^2}{2} \\ B_n &= B_{n,0} + \frac{\partial B_n}{\partial n} n + \frac{\partial B_n}{\partial l} l + \frac{\partial B_n}{\partial m} m + \frac{\partial^2 B_n}{\partial l^2}\frac{l^2}{2}, && (4) \end{aligned}$$

in addition to a single equation for $\nabla \cdot \mathbf{B} = \mathbf{0}$.

We also consider a linear model, "LB-3D" (Denton et al., 2020), with

$$B_i = B_{i,0} + \frac{\partial B_i}{\partial L} L + \frac{\partial B_i}{\partial M} M + \frac{\partial B_i}{\partial N} N, \tag{5}$$

in addition to a single equation for $\nabla \cdot \mathbf{B} = \mathbf{0}$. This is essentially the same model as the FOTE model of Fu et al. (2015).

All of these models include at least a linear dependence on m, and so are three-dimensional. 2D versions of these models, Q-2D, RQ-2D, and LB-2D, eliminate all m-dependent terms from the 3D versions (Denton et al., 2020). (A 2D version for the CQ-3D model would be the same as Q-2D, since these models only differ because of the $\partial^2 B_i/\partial m^2$ terms.) Table 1 summarizes the characteristics of the various models discussed in this paper. The terms in the header of Table 1 are expressed using l-m-n coordinates, but all the models can also be evaluated in terms of L-M-N coordinates, and we will explore that option below.

3 Reconstruction of simulation data

3.1 Simulation data

The simulation data that we will use are from the particle in cell simulation of symmetric (across the current sheet) magnetic reconnection by Liu et al. (2019). The purpose of this simulation was to study how magnetic reconnection develops when the region of a thin current sheet is limited in the reconnection M direction (the "out of plane" direction normal to the reconnection L-N plane). A two-dimensional reconnection plane contains an X point, which is the magnetic null in the B_L and B_N components. In three dimensions, the X point is extended into an X line in the M direction.

Figure 1 shows the magnetic field at three different values of M. Because the simulation data files are so big, time-resolved field data were not saved, so we are using a snapshot of the simulation fields at one time. Four virtual spacecraft move through the simulation with a velocity (3, 2, 1) d_i in L-M-N coordinates, where d_i is the ion inertial length $\equiv c/\omega_{\rm pi} = \sqrt{\frac{m_{\rm i}}{n_{\rm i}e^2\mu_0}}$, where $\omega_{\rm pi}$ is the ion (or proton) plasma frequency, $m_{\rm i}$ is the ion mass, $n_{\rm i}$ is the ion density, e is the proton charge, μ_0 is the magnetic vacuum permeability, and time is dimensionless. Since the velocity is constant, the time of flight of our virtual spacecraft corresponds directly to distance traveled. We use the N coordinate for the time. That is, at $t = 0$, $N = 0$ d_i, indicating that the centroid of the spacecraft is at center of the current sheet.

The virtual spacecraft move along the diagonal lines from the bottom left to top right in Figure 1; the colored circles show the positions of the spacecraft in each panel. At the same time, they are moving into the page, that is, in the positive M direction. Here only, L, M, and N are measured relative to the fixed center of the simulation; elsewhere, they will be measured from the centroid of the virtual spacecraft. The field in each panel corresponds to the field at the M value of the centroid of the spacecraft, so that the centroid M value is greater for Figure 1c (-5.5 d_i) than for Figure 1a (-12.5 d_i). Note that at $L = 0$, the current sheet is thicker in Figure 1a, and the reconnection has progressed less, as indicated by the smaller island width on the left and right sides of the plot and the smaller values of B_M. There is also difference in the structure of B_M as M is varied (comparing Figure 1a to Figure 1c). So the virtual spacecraft are moving through a structure that is really three-dimensional, though the gradient in the M direction is significantly smaller than that in the reconnection plane.

The simulation proton to electron mass ratio was 75. The simulation grid point spacing was 0.04 d_i and the separation between the virtual spacecraft is significantly larger, 0.5 d_i.

At each point in time, the magnetic field and current density are determined for each of the four virtual spacecraft. As we have done for our previous reconstructions of MMS data (Torbert et al., 2020; Denton et al., 2020, 2021), we initially smoothed the virtual spacecraft data using a boxcar average over a time interval (or displacement in N) $t_{\rm smooth}$. The amount of smoothing can make a significant difference in the results. In this study, we considered three choices, $t_{\rm smooth} = 0.4$, 0.8, and 1.6. Figure 2 shows the effects of smoothing on the fields. Note that in figures such as Figure 2 with two-part labels, e.g., "(Aa)", the uppercase letter (here "A") refers to a row of panels, whereas the lowercase letter (here "a") refers to a column of panels. Broadening of $\mathbf{B}$ and broadening and decrease of the magnitude of $\mathbf{J}$ occurs with greater smoothing (progressing from Figures 2A to 2D and from Figures 2E to 2H). These effects are minimal for $t_{\rm smooth} = 0.4$, but substantial for $t_{\rm smooth} = 1.6$.

Figure 3 shows the eigenvectors of MDD and Minimum Gradient Analysis (MGA) (Shi et al., 2005, 2019). This plot is made for $t_{\rm smooth} = 0.8$, but the results of MDD and MGA do not depend greatly on the smoothing (not shown). Both MDD and MGA use the matrix $\nabla\mathbf{B}$ calculated from the instantaneous data from four spacecraft (here virtual) to find eigenvectors, but MDD calculates the maximum, intermediate, and minimum gradient directions, $\mathbf{e}_n$, $\mathbf{e}_l$, and $\mathbf{e}_m$, respectively, whereas MGA finds the maximum, intermediate, and minimum variance ("MVA-like") directions, $\mathbf{e}_{l,MGA}$, $\mathbf{e}_{m,MGA}$, and $\mathbf{e}_{n,MGA}$, respectively. The L, M, and N directions that we used were the original axes of the simulation (x, y, and z, respectively, of Liu et al. (2019)). These directions differ at most by 2° from those calculated using the method of Denton et al. (2018) that makes use of the maximum gradient direction for $\mathbf{e}_N$ and the maximum variance direction for $\mathbf{e}_L$.

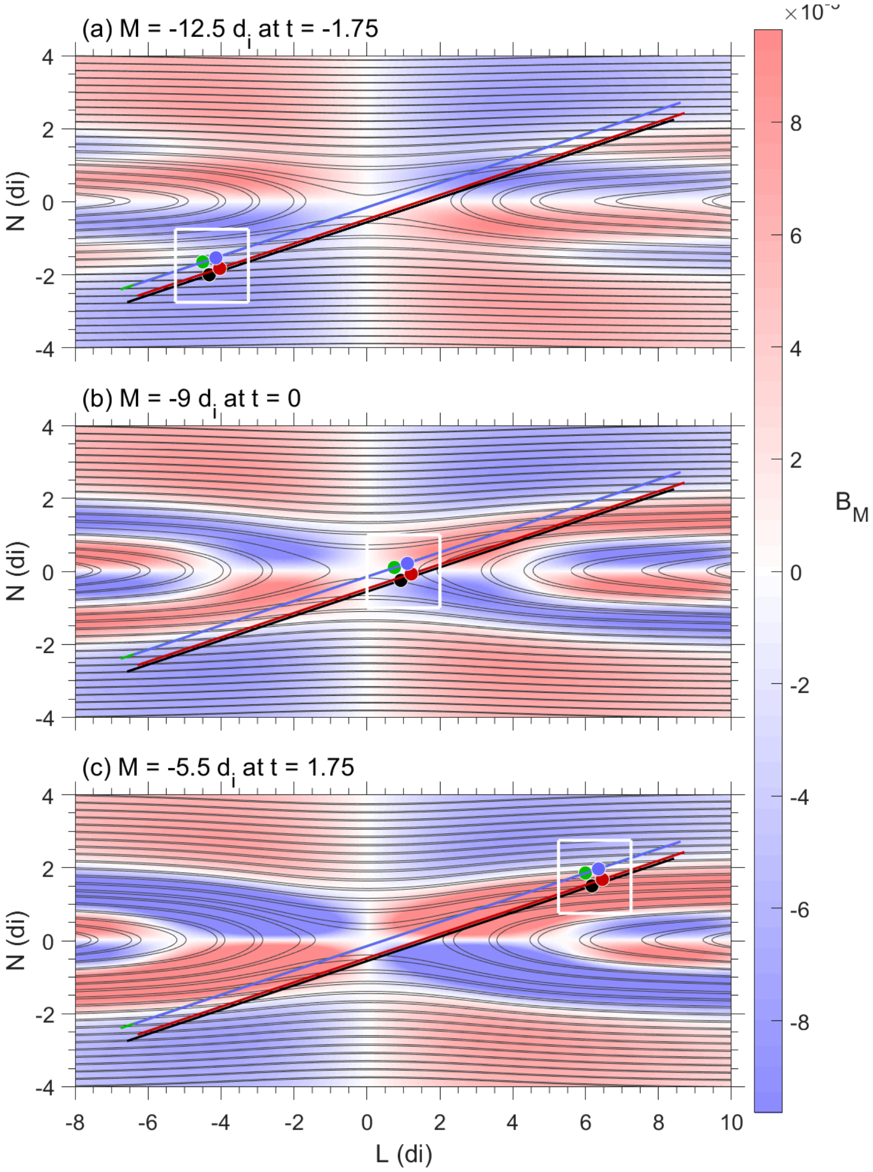

Figure 1. Magnetic field from the simulation of Liu et al. (2019). (a–c) show the simulation magnetic field at (a) $M = -12.5\ d_i$ at time $t = -1.75$, (b) $M = -9\ d_i$ at time $t = 0$, and (c) $M = -5.5\ d_i$ at time $t = 1.75$, where M was measured relative to the central M value of the simulation. Streamlines of the L and N components of the magnetic field in the L-N plane are shown by the black curves. The color scale shows B_M, which is small compared to the reconnection magnetic field $\sim$0.25 (in the simulation normalization). The diagonal lines show the trajectories of virtual spacecraft, with black, red, green, and blue corresponding to spacecraft 1, 2, 3, and 4. The circles, using the same colors, show the positions of the spacecraft at the time t when the centroid of the spacecraft is at the M values listed above. Thus the spacecraft are moving in the positive L, N, and M directions relative to the magnetic structure.

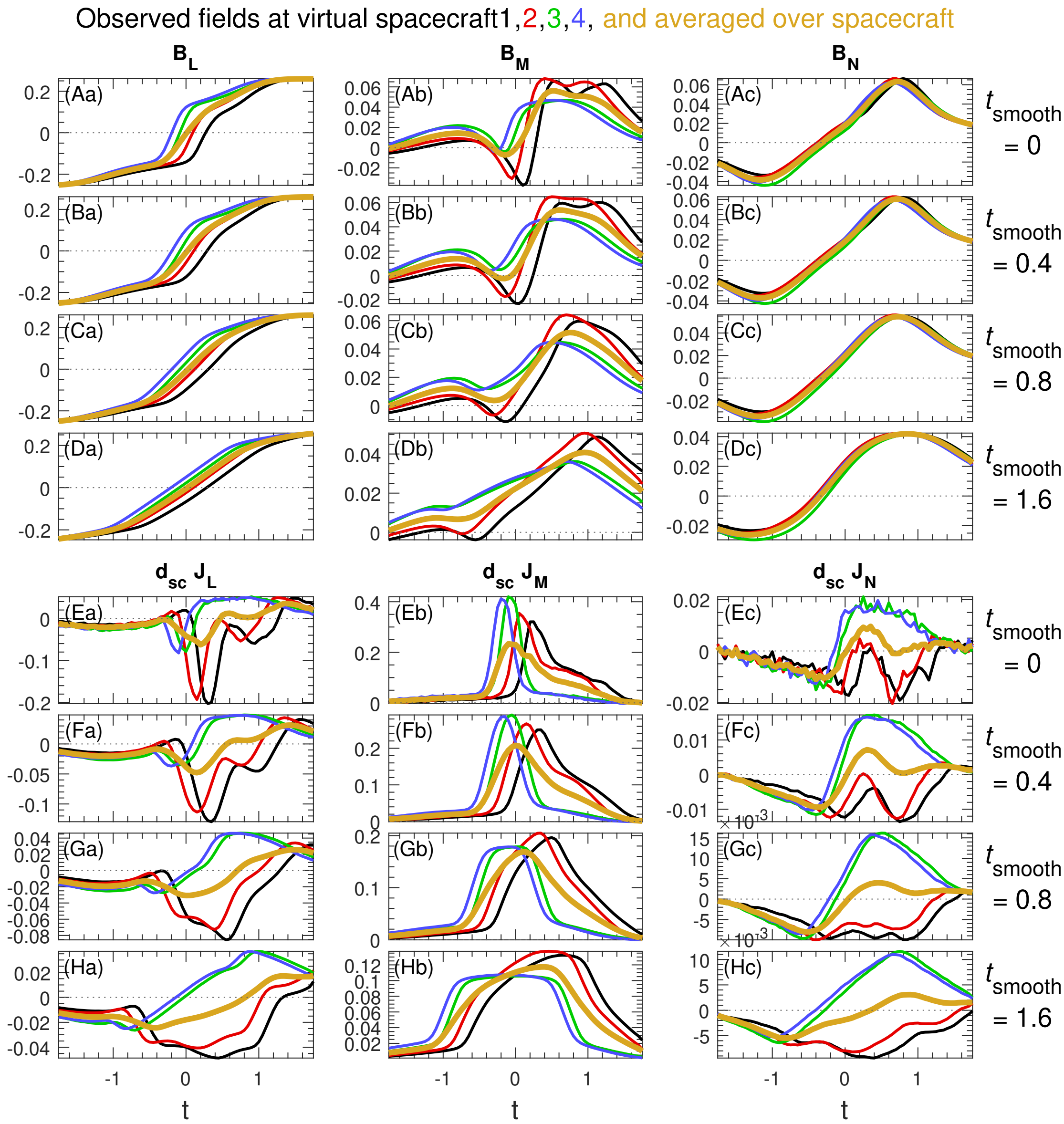

Figure 2. Input data to the reconstruction of simulation data showing the effects of smoothing. The (a) L, (b) M, and (c) N components of (A–D) the magnetic field $\mathbf{B}$, and (E–H) the product of the current density, $\mathbf{J}$, and the spacecraft spacing $d_{\rm sc}$. In the simulation, $d_{\rm sc}\mathbf{J}$ has the same units as $\mathbf{B}$. The time intervals for boxcar smoothing of the input data are shown at the right of panels c; $t_{\rm smooth} = 0$ indicates no smoothing (raw data).

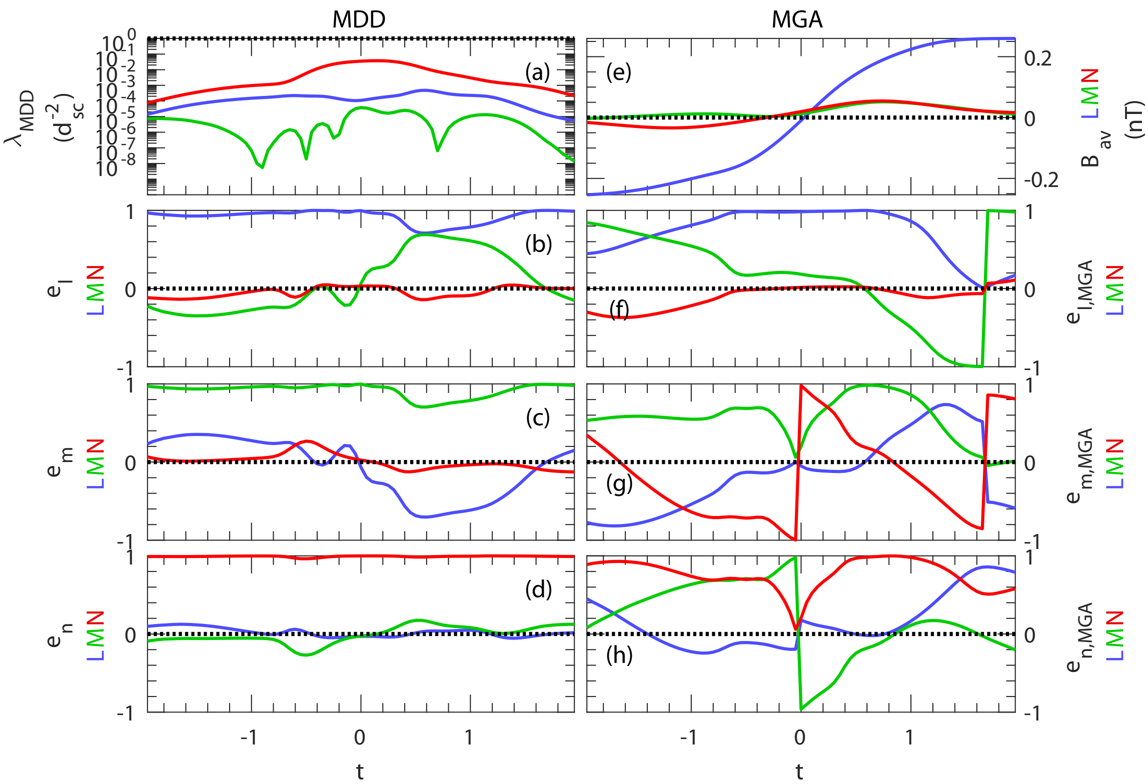

Figure 3. MDD and MGA results for simulation data. (a) MDD or MGA eigenvalues; (b–d) L, M, and N components of the MDD local gradient directions (b) $\mathbf{e}_l$, (c) $\mathbf{e}_m$, and (d) $\mathbf{e}_n$; (e) magnetic field components averaged over the four virtual spacecraft; and (f–h) MGA eigenvector directions.

Figure 3e shows the magnetic field averaged over the four spacecraft for context. The maximum gradient eigenvalue, equal to the square of the maximum gradient of the magnetic field (red curve in Figure 3a), is largest at the current sheet crossing where $B_{\mathrm{av},L}$ (blue curve in Figure 3e) reverses sign; $B_{\mathrm{av},N}$ reverses sign sooner but close to the time of the $B_{\mathrm{av},L}$ reversal (red curve in Figure 3e), showing that the spacecraft are passing close to the X line (Figure 1). Note the asymmetry in $B_{\mathrm{av},M}$ on the two sides of the current sheet, which is because the spacecraft passed to the right of the X line in Figure 1.

For much of the time, especially $t < 0$ and $t > 1.6$, $\mathbf{e}_l$, $\mathbf{e}_m$, and $\mathbf{e}_n$ are close to $\mathbf{e}_L$, $\mathbf{e}_M$, and $\mathbf{e}_N$ (Figures 3b–3d). For $0.1 < t < 1.5$, however, $\mathbf{e}_m$ is significantly different from $\mathbf{e}_M$, with a significant contribution from $\mathbf{e}_L$, as has sometimes been observed for MMS data (Denton et al., 2016, 2018). This confirms that the simulation is truly three-dimensional, although the gradients are smaller in the M direction.

The correspondence of $\mathbf{e}_{l,MGA}$, $\mathbf{e}_{m,MGA}$, and $\mathbf{e}_{n,MGA}$ with $\mathbf{e}_L$, $\mathbf{e}_M$, and $\mathbf{e}_N$ is not as strong, though for a significant portion of the time, $-0.6 < t < 0.7$, $\mathbf{e}_{l,MGA}$ is fairly close to $\mathbf{e}_L$.

3.2 Simulation reconstruction cases

We reconstructed the simulation magnetic field using the variations of method summarized in Table 2. The set of equations used in the model is indicated in the second column of Table 2. "Yes" in the fifth column of Table 2 with the "*l*-*m*-*n*?" header indicates that the local (time-dependent) MDD *l*-*m*-*n* coordinate system was used for the reconstruction. The RQ-3D and Q-3D models are normally calculated in the local *l*-*m*-*n* coordinate system, whereas the CQ-3D model is calculated in the fixed *L*-*M*-*N* coordinate system. With the complete quadratic expansion, the results are independent of the coordinate system. The same is true of the linear model, LB-3D, so we could have calculated that in the *L*-*M*-*N* coordinate system also. But we can calculate any of these models in either coordinate system. Results are always shown in the *L*-*M*-*N* coordinate system.

Cases 1–3 examine differences in results because of different smoothing. Cases 1, 2, and 3 use the RQ-3D model with $t_{\mathrm{smooth}} = 0.4$, 0.8, and 1.6, respectively (third column of Table 2). In cases 1–3, we use observations at multiple times over an interval $t_{\mathrm{input}} = t_{\mathrm{smooth}}/2$ (fourth column of Table 2). The resolution of the data is 0.05, so the number of data points used as input to the model is $t_{\mathrm{input}}/0.05+1$. For $t_{\mathrm{input}} = 0.2$, five data points are used. Using $t_{\mathrm{input}} = t_{\mathrm{smooth}}/2$ does not effectively increase the amount of smoothing, and yields slightly better reconstructions than are found using fewer observation times (not shown).

Cases 4–6 show results using input data from a single time (Denton et al., 2020), so $t_{\mathrm{input}} = 0$.

Using the multiple-time input method with a finite time interval, we solve for the structure velocity. The velocity is listed in the rightmost 3 columns of Table 2; the notation "NA" for not applicable indicates that the velocity component is not calculated. For cases 1–3 and 7–10, we solve only for the l and n (for RQ-3D or Q-3D models) or L and N (for the CQ-3D model) components of the velocity. This choice is indicated in the fifth column of Table 2 labeled "$v_{m/M}$?", where "No" in that column indicates that the m or M component is not calculated. The motivation for not calculating the m or M component is that that component of the calculated velocity is not very accurate, as we will show below. Although we calculate l and n components of the structure velocity for the RQ-3D and Q-3D methods, we convert these to L, M, and N components for the purposes of comparing to the known structure velocity. Thus for the RQ-3D or Q-3D models, we find a small velocity component in the M direction (e.g., Table 2, case 8),

Table 2. Simulation reconstruction cases

Case	Model	$t_{\rm smooth}$[a]	$t_{\rm input}$[b]	*l-m-n*?[c]	$v_{{\rm str},m/M}$?[d]	$d\mathrm{B}_{\rm err,av}$[e] ($R = 0.35d_{\rm sc}$)	$d\mathrm{B}_{\rm err,av}$[e] ($R = 1d_{\rm sc}$)	$d\mathrm{B}_{\rm err,av}$[e] ($R = 2d_{\rm sc}$)	Median velocity from polynomial reconstruction[f] $v_{{\rm str},L}$	$v_{{\rm str},M}$	$v_{{\rm str},N}$
1	RQ-3D	0.4	0.2	Yes	No	0.099	0.14	0.61	-2±0.88	-0.012±0.7	-0.9±0.2
2	RQ-3D	0.8	0.4	Yes	No	0.18	0.15	0.33	-2.2±0.67	-0.029±0.8	-0.93±0.18
3	RQ-3D	1.6	0.8	Yes	No	0.29	0.25	0.25	-2.2±0.81	-0.15±0.93	-0.85±0.18
4	LB-3D	0.8	0	Yes	NA	0.19	0.19	0.36	NA	NA	NA
5	RQ-3D	0.8	0	Yes	NA	0.18	0.15	0.38	NA	NA	NA
6	Q-3D	0.8	0	Yes	NA	0.18	0.18	0.55	NA	NA	NA
7	LB-3D	0.8	0.4	Yes	No	0.2	0.19	0.34	-2.2±0.6	0.0019±0.81	-0.96±0.13
8 (=2)	RQ-3D	0.8	0.4	Yes	No	0.18	0.15	0.33	-2.2±0.67	-0.029±0.8	-0.93±0.18
9	Q-3D	0.8	0.4	Yes	No	0.18	0.15	0.36	-2.3±0.44	-0.033±1.1	-0.96±0.12
10	CQ-3D	0.8	0.4	No	No	0.18	0.16	0.4	-2.3±0.47	NA	-0.98±0.1
11	LB-3D	0.8	0.4	Yes	Yes	0.2	0.19	0.34	$-1.5\times10^{11}\pm3.8\times10^{12}$	$5.4\times10^{11}\pm1.3\times10^{13}$	$-1.3\pm8.9\times10^{11}$
12	RQ-3D	0.8	0.4	Yes	Yes	0.18	0.15	0.35	$-2.5\pm1.3\times10^{12}$	$-4.9\pm4.3\times10^{12}$	$-0.89\pm1.9\times10^{11}$
13	Q-3D	0.8	0.4	Yes	Yes	0.18	0.15	0.37	-2.6±0.35	0.98±1.5	-1.1±0.093
14	CQ-3D	0.8	0.4	No	Yes	0.18	0.15	0.38	-2.5±0.38	0.83±1.5	-1.1±0.098
15	LB-3D	0.8	0.4	No	No	0.2	0.19	0.34	-2.5±0.39	NA	-1±0.086
16	RQ-3D	0.8	0.4	No	No	0.18	0.15	0.32	-2.3±0.4	NA	-0.94±0.12
17	Q-3D	0.8	0.4	No	No	0.18	0.15	0.36	-2.5±0.45	NA	-1±0.1
18 (=10)	CQ-3D	0.8	0.4	No	No	0.18	0.16	0.4	-2.3±0.47	NA	-0.98±0.1
19	LB-2D	0.8	0.4	Yes	No	0.2	0.19	0.34	-2.2±0.49	-0.0055±0.85	-0.96±0.13
20	RQ-2D	0.8	0.4	Yes	No	0.18	0.15	0.34	-1.8±0.64	-0.04±0.71	-0.97±0.18
21	Q-2D	0.8	0.4	Yes	No	0.18	0.16	0.35	-2.2±0.5	-0.041±1.1	-1±0.073
22	LB-2D	0.8	0.4	No	No	0.2	0.19	0.33	-2.4±0.42	NA	-1±0.096
23	RQ-2D	0.8	0.4	No	No	0.18	0.15	0.32	-2.3±0.47	NA	-0.92±0.084
24	Q-2D	0.8	0.4	No	No	0.18	0.15	0.32	-2.6±0.32	NA	-0.98±0.055
25 (=7)	LB-3D	0.8(+Sim)[e]	0.4	Yes	No	**0.2**	**0.19**	**0.34**	-2.2±0.6	0.0019±0.81	-0.96±0.13
26 (=8)	RQ-3D	0.8(+Sim)[e]	0.4	Yes	No	**0.062**	**0.075**	**0.31**	-2.2±0.67	-0.029±0.8	-0.93±0.18
27 (=9)	Q-3D	0.8(+Sim)[e]	0.4	Yes	No	**0.059**	**0.085**	**0.35**	-2.3±0.44	-0.033±1.1	-0.96±0.12
28 (=10)	CQ-3D	0.8(+Sim)[e]	0.4	No	No	**0.18**	**0.16**	**0.4**	-2.3±0.47	NA	-0.98±0.1

[a]Time interval (or N displacement) for smoothing of spacecraft **B** and **J** as input to model
[b]Time interval (or N displacement) for input to the model; 0 for method of Denton et al. (2020); the number of data points used as input to the model is $t_{\rm input}/0.05+1$
[c]"Yes" indicates that we rotate into the *l-m-n* coordinate system to calculate the reconstruction parameters
[d]"Yes" indicates that the m or M velocity component is calculated; "NA" (not applicable) if no velocity components are calculated
[e]Error parameter defined in (6) averaged from $t=-0.4$ to 0.4 at radius indicated; for cases 25–28, it is calculated with smoothed simulation data as described in the text
[f]The exact velocity is ($v_{{\rm str},L}$,$v_{{\rm str},M}$,$v_{{\rm str},N}$) = (-3,-2,-1); "NA" (not applicable) for velocity components not calculated

but not for the CQ-3D model that is calculated using an expansion in the L, M, and N coordinates (e.g., Table 2, case 10).

For cases 11-14, we solve for the three-dimensional structure velocity, as indicated by “Yes” in the sixth column of Table 2 labeled “$v_{\mathrm{str},m/M}$?”.

Cases 15–18 are like cases 7–10 (multiple times for input, but not calculating the m or M velocity component), except that all the models (even RQ-3D and Q-3D) are evaluated in the L-M-N coordinate system, as indicated by “No” in the fifth column of Table 2 with the “l-m-n?” header. So for the Q-3D model, for instance, the $\partial^2 B_i/\partial M^2$ rather than $\partial^2 B_i/\partial m^2$ dependence is not included in the model.

Cases 19–21 show results for 2D versions of the models. Cases 19–21 are evaluated in the l-m-n coordinate system as indicated by “No” in the fifth column of Table 2 with the “l-m-n?” header. So for these cases, none of the models have any m dependence. Cases 22–24 are similar except evaluated in the L-M-N coordinate system, so that none of the models have any M dependence.

The seventh, eighth, and ninth columns of Table 2 show the average (mean) error parameter $dB_{\mathrm{err,av}}$, with

$$dB_{\mathrm{err}} = \frac{|\mathbf{B}_{\mathrm{mod}} - \mathbf{B}_{\mathrm{sim}}|}{B_{\mathrm{sim,max}}}, \tag{6}$$

at three radial distances from the centroid of the spacecraft positions, where $\mathbf{B}_{\mathrm{mod}}$ is the reconstruction model field, $\mathbf{B}_{\mathrm{sim}}$ is the simulation field, and $B_{\mathrm{sim,max}}$ is the maximum magnitude of the simulation field in the reconstructed region, which has the shape of a cube with L/d_{sc}, M/d_{sc}, and N/d_{sc} varying from -2 to +2. Values of $dB_{\mathrm{err,av}}$ are shown for radii of $0.35d_{\mathrm{sc}}$, $1d_{\mathrm{sc}}$, and $2d_{\mathrm{sc}}$ from the centroid of the spacecraft within the three-dimensional volume. The averaging is done over different locations at the radii specified (roughly within a spherical shell of width 0.1 d_{sc}) and over the time interval $t = -0.4$ to 0.4. That is the time interval over which the errors are greatest. For a perfect reconstruction, the values of $dB_{\mathrm{err,av}}$ would be zero. A value of $dB_{\mathrm{err,av}}$ equal to unity would mean that the reconstructed magnetic field is far from the simulation field. The radius $0.35d_{\mathrm{sc}}$ is less than the distance to the individual spacecraft at $0.61d_{\mathrm{sc}}$ and within the spacecraft tetrahedron. The radius of $1d_{\mathrm{sc}}$ is outside the spacecraft tetrahedron, and the distance $2d_{\mathrm{sc}}$ is significantly farther away.

Cases 25–28 in Table 2 are the same as cases 7–10 except that $dB_{\mathrm{err,av}}$ is calculated using spatially smoothed simulation data, as described in section 5.7. So the only different numbers in Table 2 for cases 25–28 are the boldface numbers showing $dB_{\mathrm{err,av}}$ values.

3.3 Reconstruction results considering differences in smoothing

Figure 4 compares model (solid curves) and the smoothed virtual spacecraft data (dotted curves) components of $\mathbf{B}$ and $d_{\mathrm{sc}}\mathbf{J}$ for simulation reconstruction case 2 in Table 2. This case used the RQ-3D model with $t_{\mathrm{smooth}} = 0.8$ and $t_{\mathrm{input}} = 0.4$ and solved for the three-dimensional structure velocity without calculation of $v_{str,m}$. Comparing the solid and dotted curves, the data was fairly well described by the model. The agreement is least good for J_N, but note that the values of J_N are very small. Other cases using the RQ-3D model show comparable agreement. Much better agreement is achieved with the Q-3D and CQ-3D models because of the greater number of parameters in those models.

Agreement of the model and simulation fields at the spacecraft positions, as shown in Figure 4, is a consistency check for the model, but it does not show that the reconstructions accurately represent the simulation fields away from the spacecraft positions.

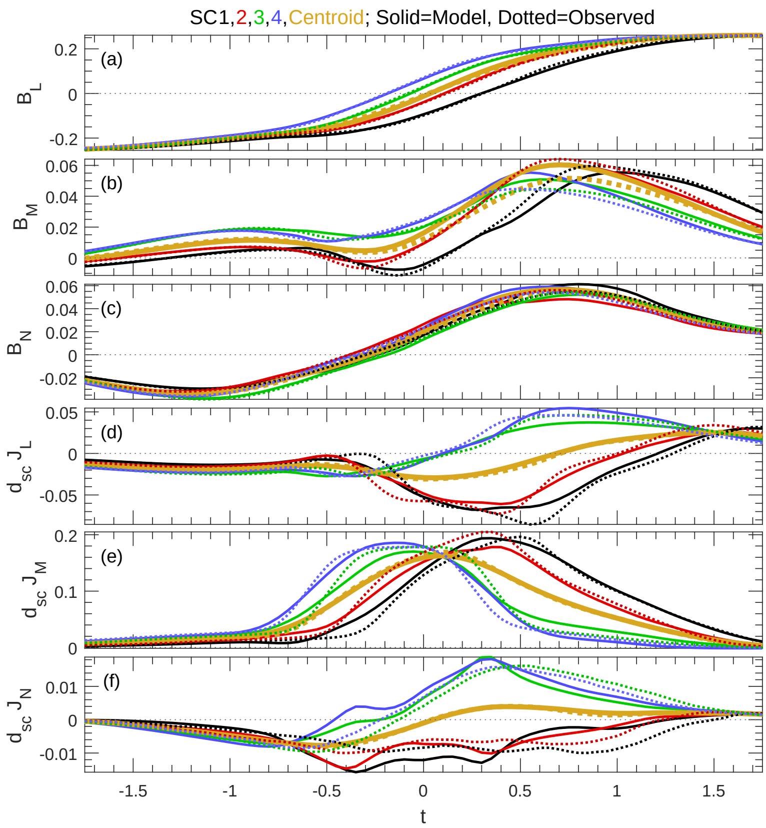

Figure 4. Comparison of model and virtual spacecraft data. Model (solid) and virtual spacecraft data (dotted) (a–c) magnetic field and (d–f) current density components multiplied by d_{sc} for simulation reconstruction case 2 in Table 2.

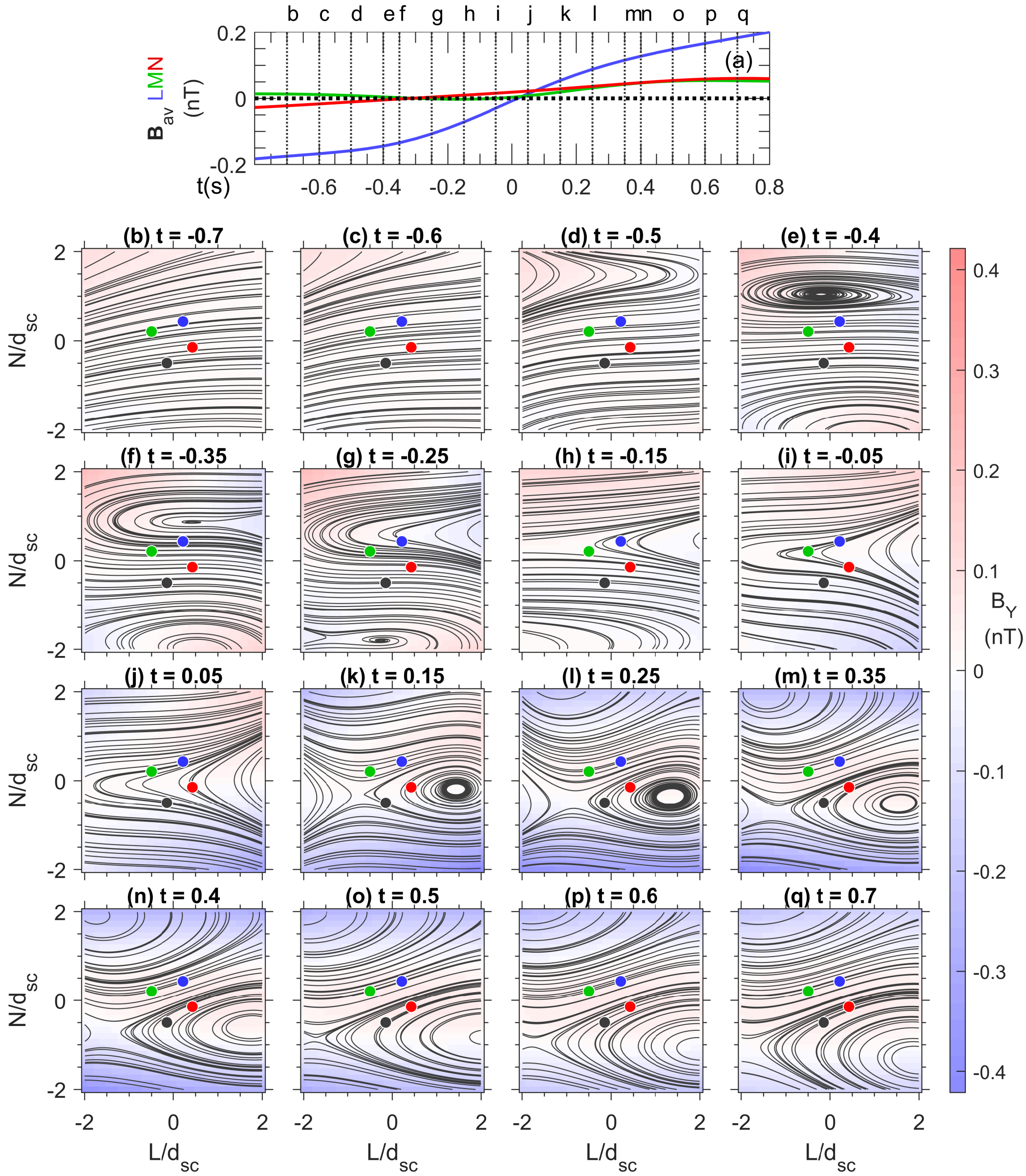

Figure 5. Reconstruction magnetic field in the L-N plane for reconstruction case 1. (a) Magnetic field averaged over the four virtual spacecraft, $\mathbf{B}_{\mathrm{av}}$, versus time showing the times of the two-dimensional representations of the magnetic field in panels b–q. (b–q) Reconstructed magnetic streamlines in the L-N plane (black) and magnetic field into the plane of the page, B_M (color scale). The positions of the virtual spacecraft relative to the spacecraft centroid (origin of each panel) are indicated by the black, red, green, and blue circles for spacecraft 1, 2, 3, and 4.

Figure 5 shows the reconstructed magnetic field for case 1 during the time that the virtual spacecraft come close to the reconnection X line. The X line does not progress with constant velocity past the spacecraft, as it should based on how we created the virtual spacecraft data. Furthermore, there are unrealistic features (comparing these reconstructions to Figure 1), like the island at $t = -0.4$. The sudden appearance of this island (movie S1 in the Supplementary Information) indicates inconsistency in the reconstructions.

With t_{smooth} increased to 0.8 (case 2 in Table 2), there is much more consistency in the reconstructions (movie S3 in the Supplementary Information for case 8 equivalent to case 2). The magnetic structure in the L-N plane is always in relatively good agreement with that of Figure 1, and the X line of the magnetic structure moves past the spacecraft with a nearly uniform velocity. While it is possible that the magnetic structure would evolve during the time period that the spacecraft moved past the X line for an event observed by MMS (see, e.g. Denton et al., 2020), one should be cautious in coming to such an interpretation because of the inaccuracies in reconstruction. And there should be a reasonable physical explanation for the evolving structure. The consistency of the reconstructions for case 2 is evidence that supports the validity of these reconstructions.

Figure 6 compares the reconstruction magnetic field for case 2 with the simulation field in the L-N plane, where the simulation field is calculated for each time at the M value of the centroid of the spacecraft positions. There are some unrealistic features. For instance, the model shows a small island in the upper left of the top panel of Figure 6c and the X line stays in the reconstruction domain at late times, whereas the simulated fields show that the X line should be outside the field of view (Figure 6f–6h). Also, there are significant differences in the structure of B_M, as will be discussed below. But overall, the reconstruction does a good job of representing the magnetic structure. And the velocity of the X line does appear to be accurate when the X line is closest to the spacecraft (Figure 6c–6e).

Now consider the error parameter $dB_{\mathrm{err,av}}$ for cases 1–3 in Table 2. At a radius from the spacecraft centroid, R, equal to $0.35d_{\mathrm{sc}}$ and $1d_{\mathrm{sc}}$, these error parameters are smallest for case 1 with the smallest value of $t_{\mathrm{smooth}} = 0.4$. This is because the reconstruction is based on the temporally smoothed fields. The reconstruction yields a smoother gradient in the dominant component B_L with respect to N than is present in the simulation. So the fields within and close to the spacecraft positions are more accurate with less smoothing. But with a moderate increase in error at the small values of R, we can achieve a big reduction in the errors at $R = 2d_{\mathrm{sc}}$ by using $t_{\mathrm{smooth}} = 0.8$ (case 2) (reduction of $dB_{\mathrm{err,av}}$ from 0.61 to 0.33). Furthermore, as shown in movie S3 and Figure 6, case 2 yields reconstructions with consistent magnetic structure which appear to be realistic. Case 3, with $t_{\mathrm{smooth}} = 1.6$ has a further decrease in the errors at $R = 2d_{\mathrm{sc}}$ at the expense of greater error at small radii. But from now on, all results will use the moderate amount of smoothing, $t_{\mathrm{smooth}} = 0.8$, with a moderate distortion in the magnetic field and current density (Figure 2).

3.4 Results for different models using a single observation time for input

Cases 4–6 in Table 2 show the simulation results using observations at a single time (method of Denton et al. (2020)). Except for case 6 using the Q-3D model, the errors are comparable to, but somewhat greater than, those of case 2 using the multiple-time input method. The errors for the Q-3D model are significantly larger at $R = 2d_{\mathrm{sc}}$ ($dB_{\mathrm{err,av}} =$ 0.55 compared to 0.38 for the RQ-3D model of case 5) because of overfitting.

One might think that the Q-3D model would do better than the RQ-3D model within the spacecraft tetrahedron if there were less smoothing, because the Q-3D model, similar to the method of Torbert et al. (2020), almost exactly fits the model to the space-

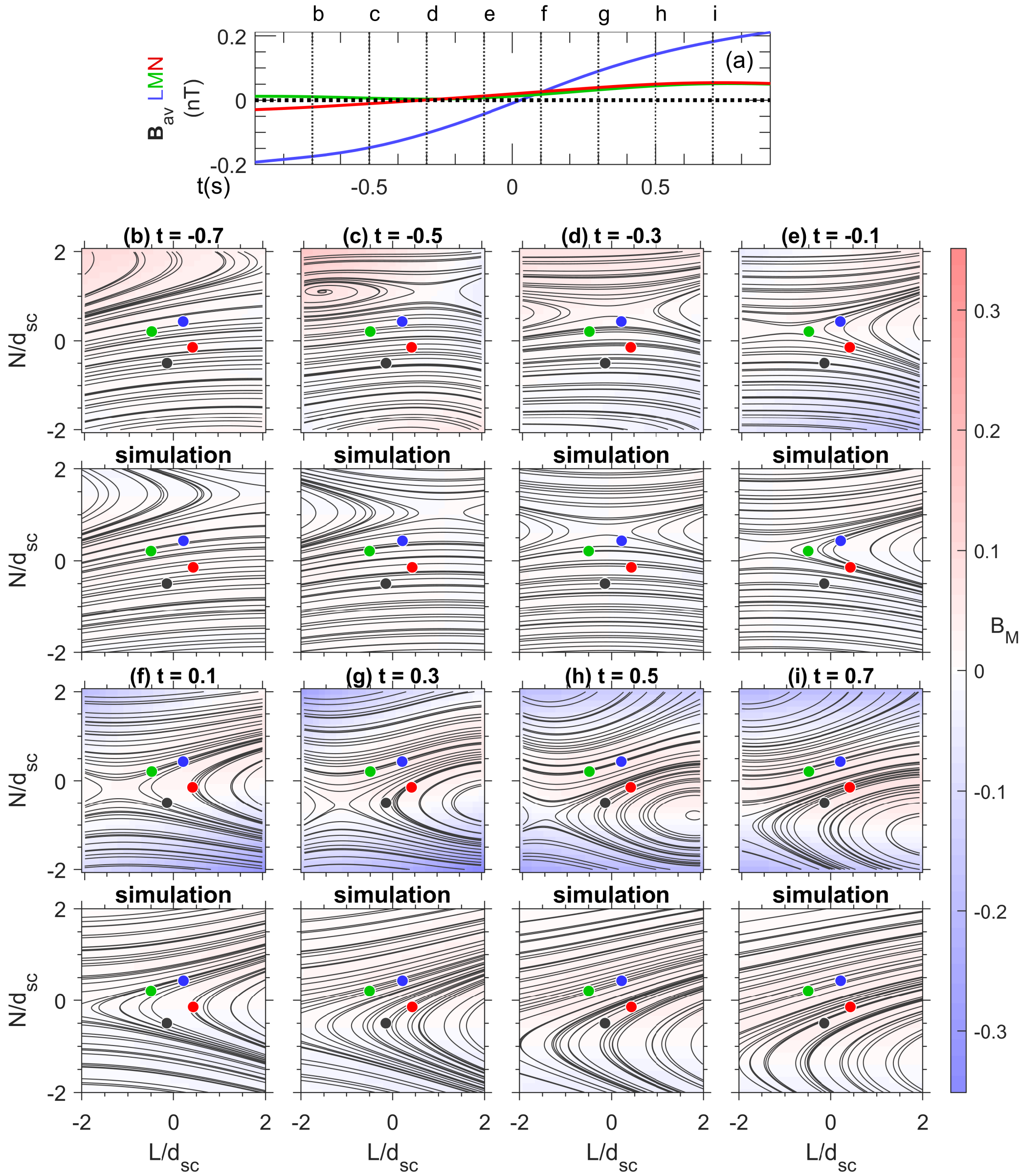

Figure 6. Comparison of reconstruction and simulation magnetic field in the L-N plane for simulation reconstruction case 2. (a) Magnetic field averaged over the four virtual spacecraft as in Figure 5. (b–i) In each pair of vertically arranged panels, reconstructed (top, with time label) and simulation (bottom, labeled "simulation") magnetic streamlines in the L-N plane (black) and magnetic field into the plane of the page, B_M (color scale).

craft observations at the spacecraft locations (Denton et al., 2020). Using $t_{\rm smooth} = 0.4$ and $t_{\rm input} = 0.2$, the Q-3D model does yield a small value of $dB_{\rm err,av} = 0.092$ inside the tetrahedron at $R = 0.35d_{\rm sc}$ (case not listed in Table 2). But the RQ-3D model yields almost the same value, 0.099 (case 1 in Table 2). And the Q-3D model with $t_{\rm smooth} = 0.4$ and $t_{\rm input} = 0.2$ yields values of $dB_{\rm err,av}$ that are significantly larger than those of the RQ-3D model at both $R = 1d_{\rm sc}$ and $2d_{\rm sc}$, 0.21, and 0.95, respectively, compared to 0.14 and 0.61 for case 1.

3.5 Results for different models using multiple observation times for input

Cases 7–10 show results for the multiple-time input method but using different models. Note that case 8 is the same as case 2, but repeated in Table 2 for easier comparison to cases 7, 9, and 10. The errors are slightly smallest for case 8 (= case 2) for the RQ-3D model, though there is not a great difference in results as the model is varied. Figure 7 is like Figure 6, except for case 10 for the complete quadratic CQ-3D model. See also movie S5 for case 10 in the supplementary information. Figure 7 shows that it is possible to use a complete expansion by making use of the greater number of observations from a finite time interval.

In some respects, the reconstructions in the L-N plane shown in Figure 7 for the CQ-3D model are more realistic than those in Figure 6 for the RQ-3D model. For instance, note that the reconstructed fields like the simulation fields in Figure 7c (top and bottom panels, respectively) do not include an O point and that the X line is to the left of the field-of-view for both reconstructed and simulation fields in Figure 7h. The CQ-3D model also has the advantage that no rotations are required.

The errors for case 10 as indicated by $dB_{\rm err,av}$ are somewhat greater than those for the RQ-3D model (case 8), but not much greater. As noted above, this is in contrast to the results using a single time of observation as input to the model, for which the errors at $R = 2d_{\rm sc}$ for the Q-3D model, omitting only the $\partial^2 B_i/\partial m^2$ terms, were significantly greater than those of the RQ-3D model (comparing cases 5 and 6 in Table 2). Simply put, a model with more parameters requires more input data.

To get a better understanding of the errors from the model, we show in Figure 8 2D cuts through 3D space of B_L, B_M, and B_N at $t = -0.3$, corresponding to Figure 6d. The reconstruction model fields are shown in Figures 8a, 8d, and 8g, the simulation fields are shown in Figures 8b, 8e, and 8h, and the model fields minus the simulation fields are shown in Figures 8c, 8f, and 8i. Figures 8j show the error parameter $dB_{\rm err}$. The color scale in each panel can be interpreted using the color bars at the bottom of the plot. Note that the values of B_L are much larger than those of B_M and B_N, as indicated by the scales on the color bars.

Consider first the L-N cuts in Figure 8B. Figures 8Ba–8Bc show that the model preserves the simulation gradient of B_L with respect to N, but the model gradient is broader. The simulation gradient of B_N with respect to L is not so large (Figure 8Bh), and at $N = 0$, the model B_N (Figure 8Bh) agrees with the simulation B_N (Figure 8Bg). But B_N varies too much with respect to N(Figure 8Bg). This may be related to the slight variation of the larger B_L with respect to L, so that B_N varies with N so as to make $\nabla\cdot$ $\mathbf{B}$ equal to zero. The fact that $B_L = B_N = 0$ (white color in Figure 8) occurs at the same values of N and L, respectively, for both model and simulation (Figures 8Ba, 8Bb, 8Bg, and 8Bh), indicates that the model correctly predicts the position of the X line, as was already shown in Figure 6d.

Figures 8Bd and 8Be show a big difference between the model and simulation B_M in the L-N plane. The model does not correctly represent the quadrupolar structure. This is understandable considering that the virtual spacecraft passed under the X line

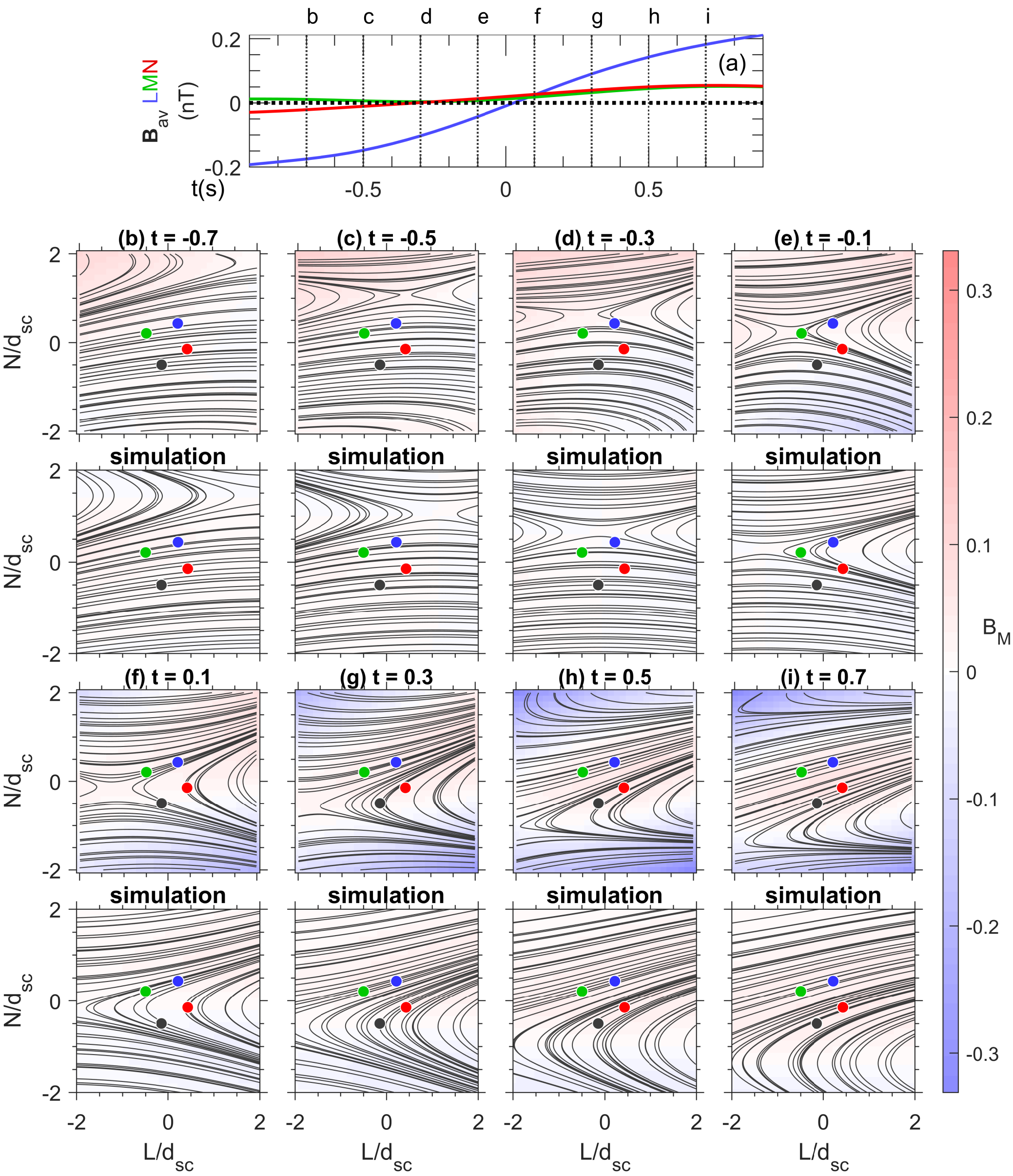

Figure 7. Comparison of reconstruction and simulation magnetic field in the L-N plane for simulation reconstruction case 10. This plot is like Figure 6, except for case 10.

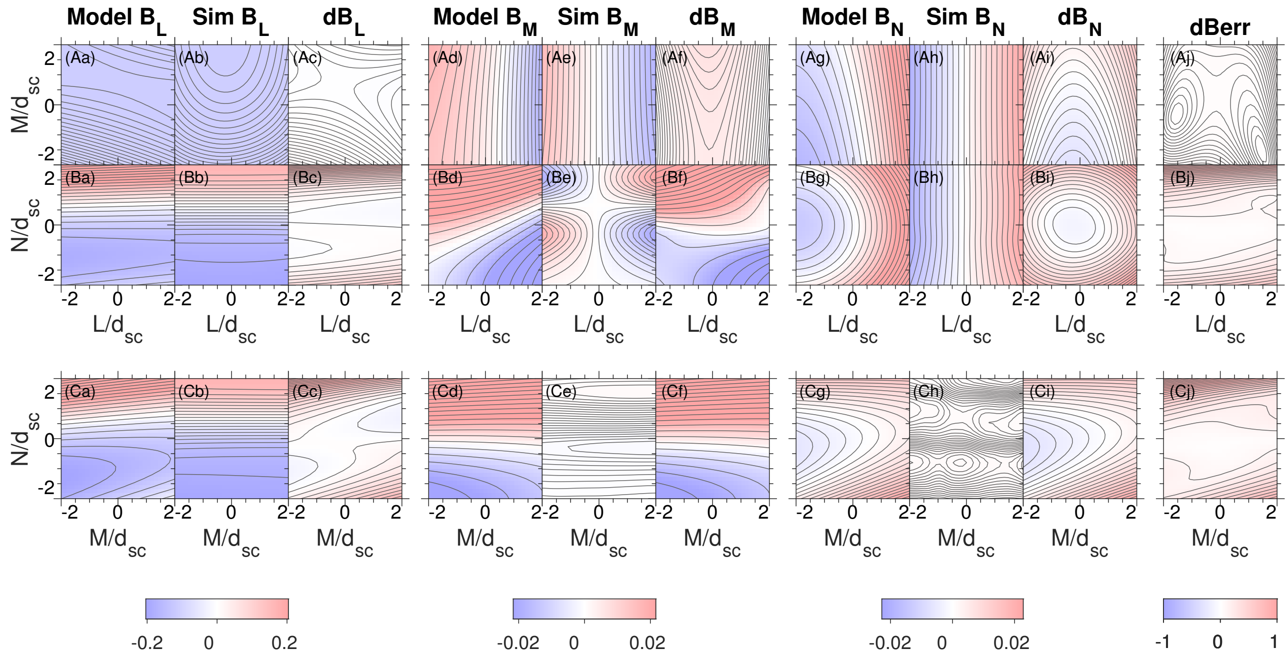

Figure 8. Two dimensional cuts of the model and simulation magnetic field for reconstruction case 2 in Table 2. In rows A–C, 2D cuts in the (A) L-M (at $N = 0$), (B) L-N (at $M = 0$), and (C) M-N (at $L = 0$) planes of various quantities. In columns a–c, the L component of the magnetic field of (a) the reconstruction model, (b) the simulation field, and (c) the model field minus the simulation field, dB_L. Columns d–f and g–i are like a–c, except that the components plotted are (d–f) the M components and (h–i) the N components. In column j, the error parameter dB_{err} defined in the text is plotted.

and did not sample the upper left quadrant of Figure 8Be. Because of this, the model has a large N dependence in the M-N plane (Figure 8Cd), whereas the simulation in that plane has B_M approximately equal to zero (Figure 8Ce).

The model also has significantly greater M dependence than the simulation. And the error parameter dB_{err} (Figures 8j) is nonzero even close to the centroid of the spacecraft positions (origin of panels in Figure 8j). These results suggest that reconstruction results should be interpreted cautiously, understanding that there may be significant errors, particularly involving dependence that is not well sampled by the spacecraft.

Figures S2–S5 in the Supplementary Information compare reconstruction and simulation fields for cases 7–10, respectively, using the format of Figure 6. Similarly, movies S2–S5 show the time variation of the reconstruction magnetic field for cases 7–10. Despite the differences in the error parameter $dB_{\text{err,av}}$ shown in Table 2, all of the models yield reasonable reconstruction results in the L-N plane.

3.6 Velocity from the reconstruction

As previously mentioned, the exact structure velocity (relative to the spacecraft) used to create the virtual spacecraft data was ($v_{\text{str},L}$,$v_{\text{str},M}$,$v_{\text{str},N}$) = (-3,-2,-1). For each case in Table 2 using the multiple-time input method (all cases other than 4–6), the method yields an estimate of the structure velocity (last 3 columns of Table 2).

Figure 9 shows the inferred velocity from the reconstruction (solid curves) versus time for case 2. We also show the velocity from the Spatio-Temporal Difference (STD) method Shi et al. (2006) (dotted curves). Clearly the velocities from the reconstruction and from STD are very similar.

For STD, we only calculated components of the velocity in the local l and m directions. For cases 1–3 and 7–10, we also assumed that the structure velocity only had l and n (or L and N for the CQ-3D model) components. Therefore the value of $v_{\text{str},m}$ in Figure 9b is zero (dotted and solid curves). But the velocity components in the M direction are nonzero because $\mathbf{e}_l$ sometimes has a significant M component, as shown in Figure 3c. Nevertheless, the $v_{\text{str},M}$ component cannot be accurate since it does not include a contribution from $v_{\text{str},m}$, and $\mathbf{e}_M$ is closer to $\mathbf{e}_m$ than to $\mathbf{e}_l$ or $\mathbf{e}_n$.

Because of the large time variation of the calculated velocity, we chose to list median velocity values over the entire time interval -1.75 to 1.75 in Table 2. For the reason mentioned in the last paragraph, the values of $v_{\text{str},M}$ in the second to the last column of Table 2 are either inaccurate or not applicable for cases 1–3 and 7–10. The exact value of $v_{\text{str},L}$ is -3, but all the estimates for cases 1–3 and 7–10 yield values between -2 and -2.3. Looking at Figure 9d, the most inaccurate values of $v_{\text{str},L}$ occur around $t =$ 0.6, where $\mathbf{e}_L$ has a significant m component (Figure 3b), whereas more accurate values of $v_{\text{str},L}$ (especially those from STD) occur at $t = -0.4$, 0, and 1.7, where the m component of $\mathbf{e}_L$ is nearly zero.

Another possible cause of inaccuracy might be related to large nonlinearity of the fields. The most inaccurate values of $v_{\text{str},L}$ in Figure 9d occur at $t = \pm 0.5$, where the variation in $\mathbf{J}$ measured by the MMS spacecraft is greatest (Figure 4d–4f).

The estimates for $v_{\text{str},N}$ are more accurate. The exact value should be -1, and the estimates range between -0.85 and -0.98. It is not surprising that the most accurate component calculated is $v_{\text{str},N}$, because the gradient in the N direction is the best measured (Denton et al., 2021).

Cases 11–14 in Table 2 are like cases 7–10, except that the reconstruction method allows the structure velocity to have components in all three directions (as indicated by "Yes" in the sixth column of Table 2 labeled "$v_{\text{str},m/M}$"). The resulting velocities are

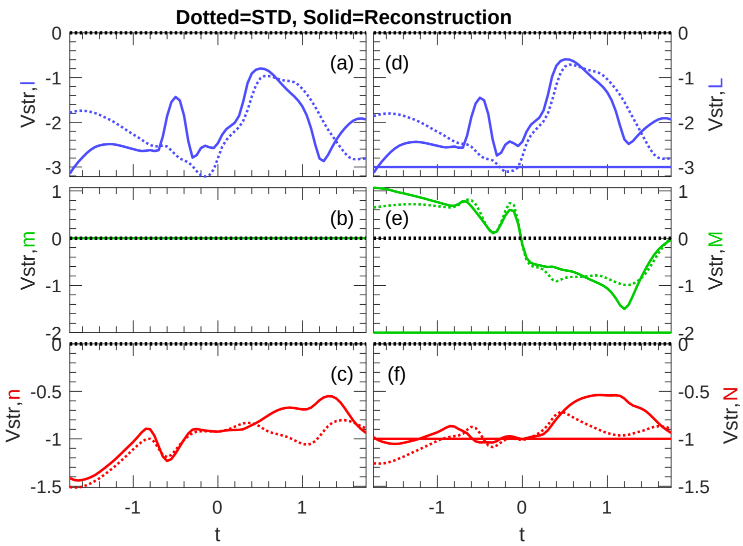

Figure 9. Inferred structure velocity for simulation reconstruction case 2. Velocity components in (a–c) the local MDD l-m-n coordinate system and (d–f) the global L-M-N coordinate system. The dotted curves show the velocity from the Spatio-Temporal Difference (STD) method (Shi et al., 2006) and the solid curves show the velocity that optimized the fit of reconstruction model and simulation values at the spacecraft locations. The exact values, $v_{\mathrm{str},L} = -3$, $v_{\mathrm{str},M} = -2$, and $v_{\mathrm{str},N} = -1$, are shown as the blue, green, and red horizontal solid lines in panels d, e, and f, respectively. For case 2, we did not calculate the m component of velocity for reconstruction or for STD, so $v_{\mathrm{str},M}$ is inaccurate.

totally inaccurate for the low order methods, LB-3D and RQ-3D (cases 11 and 12), as indicated by the huge error bars (standard deviation) for the velocity in the last three columns of Table 2. The higher order methods, Q-3D and CQ-3D (cases 13–14) have improved values for $v_{\mathrm{str},L}$, but the values for $v_{\mathrm{str},M}$ are not at all accurate (they should be -2).

3.7 Other variations of method

In cases 15–18, we calculate all the polynomial expansions in the L-M-N coordinate system rather than l-m-n. That is, in expansions such as equations (2–4), we substitute L, M, and N for l, m, and n. This choice is indicated by "No" in the column of Table 2 labeled "l-m-n?". In some cases, the results are very slightly improved (comparing, for instance, the errors at $R = 2d_{\mathrm{sc}}$ for cases 16, with $dB_{\mathrm{err}} = 0.32$, and case 8, with $dB_{\mathrm{err}} = 0.33$. The negative aspect of this approach is that one needs to be confident that the L-M-N coordinate system is appropriate. Knowing the best coordinate system is easy for this simulation, but difficult for reconnection events in space (Denton et al., 2018).

Cases 19-21 and 22–24 show results for 2D versions of the models, with cases 19–21 evaluated in the l-m-n coordinate system, and cases 22-24 evaluated in the L-M-N coordinate system. Using the l-m-n coordinate system (cases 19-21), the errors are not reduced compared to those using the 3D models (comparing cases 19–21 to cases 7–9).

Cases 22–24, 2D models evaluated in the L-M-N coordinate system, have errors that are among the lowest in Table 2. But again, use of these models would require confidence about the appropriate L-M-N coordinate system.

Taking account that larger times for smoothing result in larger errors inside the tetrahedron, because of the broadening of the gradients, we also tried doing reconstructions with small values of t_{smooth} and large values of t_{input}. These calculations do have reduced errors within the spacecraft tetrahedron, but at the expense of larger errors at $2d_{\mathrm{sc}}$ and less consistency in the reconstructed fields with respect to time.

4 Reconstruction of MMS events

4.1 Reconstruction of 27 August, 2018, MMS event

Now that we have tested our reconstructions by comparing to three-dimensional simulation data, we use the multiple-time input method to reconstruct the magnetic structure for the magnetotail reconnection event of 27 August, 2018, described by Li et al. (2021). This event occurred at 11:41 UT at (X,Y,Z) = (-21.1, 11.0, 7.5) Earth radii (R_{E}) in Geocentric Solar Ecliptic (GSE) coordinates, and the spacecraft were in a tetrahedron formation with 34 km average separation between the spacecraft (1.4 d_e, where $d_e \equiv c/\omega_{\mathrm{pe}} = \sqrt{\frac{m_{\mathrm{e}}}{n_{\mathrm{e}} e^2 \mu_0}}$ is the electron inertial length). We used Li et al.'s coordinate system, (L; M; N) = (0.97, -0.17, -0.17; 0.20, 0.96, 0.19; 0.14, -0.22, 0.97) in GSE. Special processing was required to get the current density from the FPI instrument. Because of low-energy photoelectron contamination to the electron data, we computed electron partial moments by integrating energies over 50 eV (Gershman et al., 2017). Our purpose here is not to describe this event in detail, but rather just to demonstrate our reconstruction technique. For details about this event, see the description of Li et al. (2021).

We now reconstruct the fields around the MMS spacecraft with parameters similar to that of simulation reconstruction case 2. We chose $t_{\mathrm{smooth}} = 0.5$ s, and $t_{\mathrm{input}} =$ 0.24 s (25 data points at 0.01 s resolution). We used the RQ-3D model and allowed the magnetic structure to have only l and n velocity components. The reconstructions in the L-N plane are shown in Figure 10. Li et al.'s (2021) interpretation of the data for this

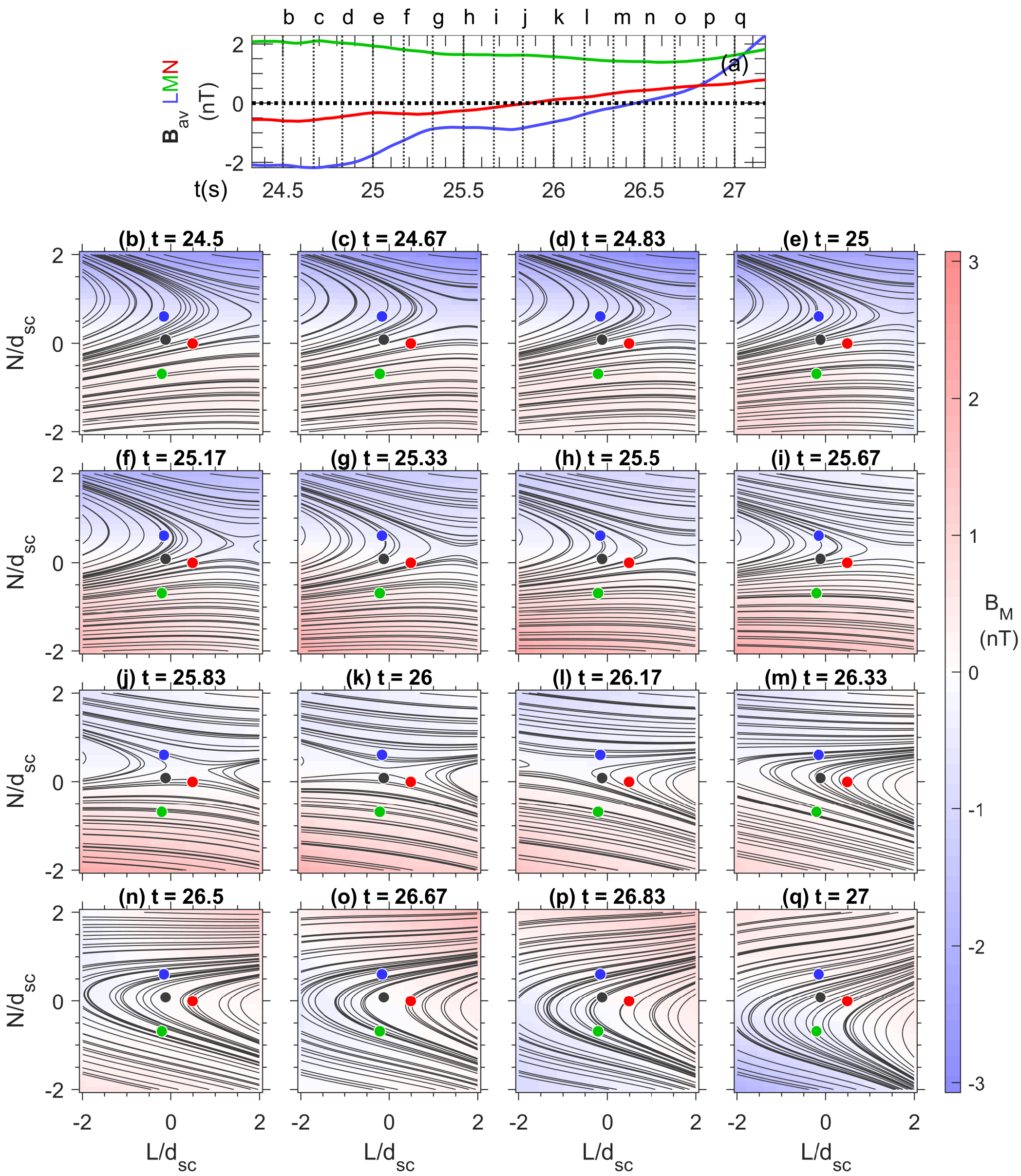

Figure 10. Reconstruction of the magnetic field for the magnetotail reconnection event observed by MMS and described by Li et al. (2021). This plot has the same format as Figure 5. The time is measured in s after 11:41 UT on 27 August, 2018.

event was that the MMS spacecraft passed mostly in the L direction right through the X line (see their Figure 1k) with closest approach by MMS1. This is exactly what we see in Figure 10. Note that in Figure 10k, MMS1 is very close to the X line. See movie S6 in the Supplementary Information for more detailed time dependence.

The inferred velocity for this event is shown in Figure 11. There are oscillations in the L and N components, but these are most often negative with average values of $v_L = -107$ km/s and $v_N = -6.5$ km/s. At some times, especially between $t = 24.6$ and 25.4 and between $t = 25.8$ and 26.3, $\mathbf{e}_m$ was almost exactly equal to $\mathbf{e}_M$ (not shown). At other times $\mathbf{e}_m$ had contributions from both $\mathbf{e}_M$ and $\mathbf{e}_L$. Therefore v_M cannot be determined, and v_L will not be exactly accurate (see subsection 3.6). The multi-time input method using the complete velocity (including v_m) could not be used in this case because the solution of the equations was numerically ill determined.

We saw in section 3.3 that the amount of smoothing could make a big difference in reconstruction results. Figure 12 shows that the raw magnetic field data for the MMS event exhibited larger fluctuations than the virtual spacecraft data for the simulation (Figure 2). Smoothing of the MMS data with $t_{\mathrm{smooth}} = 0.5$ s smoothed out those magnetic fluctuations, but the smoothing of the current density (Figure 12D as compared to Figure 12C) seems to be less than the smoothing that we recommended for the simulation data (Figure 2G as compared to Figure 2E).

The 27 August 2018 event was observed after the failure of two of the four FPI instrument sensors on MMS4, which occurred on 7 June 2018 at 12:43 UT. Because of that failure, the current density cannot be reliably calculated for MMS4, reducing the amount of input data. But because we used multiple observation times for input, and also because we used the RQ-3D model that has a reduced number of parameters, we were able to do the reconstruction without the current density from MMS4 (as would not be possible for the Q-3D or Torbert et al. (2020) models using the fields for a single observation time as input).

4.2 Reconstruction of 7 December, 2016, MMS event

Now we use the multiple-time input method to reconstruct the magnetic field for the 7 December 2016 magnetopause crossing described by Fuselier et al. (2019). This event occurred at 05:19 UT at (X,Y,Z) = (9.6, 0.7, -0.5) Earth radii (R_{E}) in Geocentric Solar Ecliptic (GSE) coordinates, and the spacecraft were in a tetrahedron formation with 6.8 km average separation between the spacecraft, equal to 0.14 d_i using the magnetosheath density (Haaland et al., 2019). We used the coordinate system (L; M; N) = (0.29 -0.37 0.88 ; -0.08 -0.93 -0.36 ; 0.95 0.03 -0.30), determined using the method of Denton et al. (2018).

We again use $t_{\mathrm{smooth}} = 0.5$ s, and $t_{\mathrm{input}} = 0.24$ s (9 data points at 0.03 s resolution), allowing the magnetic structure to have only l and n velocity components. The reconstructions in the L-N plane are shown in Figure 13. Note that here the color scale shows B_L rather than B_M, because that helps identify the current sheet crossing and because B_M was fairly constant (Figure 13a, green curve). Fuselier et al.'s interpretation was that the MMS spacecraft were far (many R_E) from the X line, and the purpose of this example is to show that we do not always see X or O points in our reconstructions. Instead, the plot shows that the magnetic structure moves downward in Figures 13b–13g, so that relative to that structure, the MMS spacecraft pass from the magnetosphere (red color in Figures 13b–13e indicating positive B_L, where $\mathbf{e}_L$ is approximately in the GSE Z direction) through the current sheet (Figures 13i–13k) and into the magnetosheath (blue color in Figures 13n–13q indicating negative B_L). See movie S7 in the Supplementary Information for more detailed time dependence.

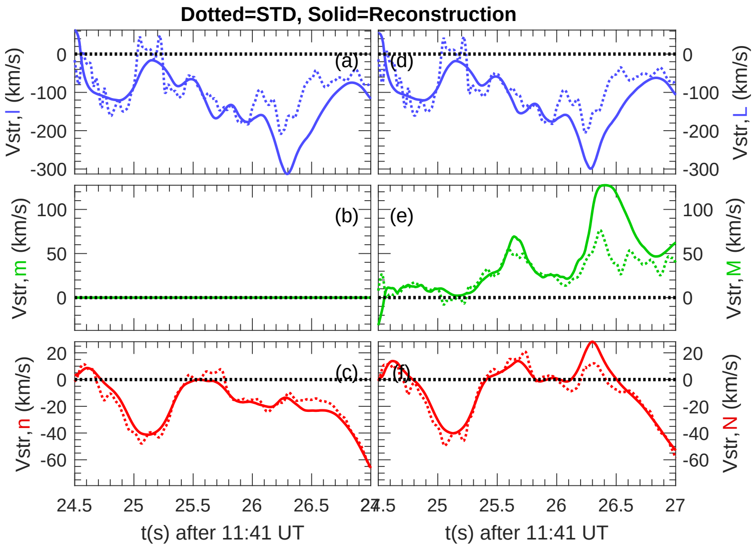

Figure 11. Inferred structure velocity for the MMS reconnection event observed on 27 August, 2018, using the same format as Figure 9.

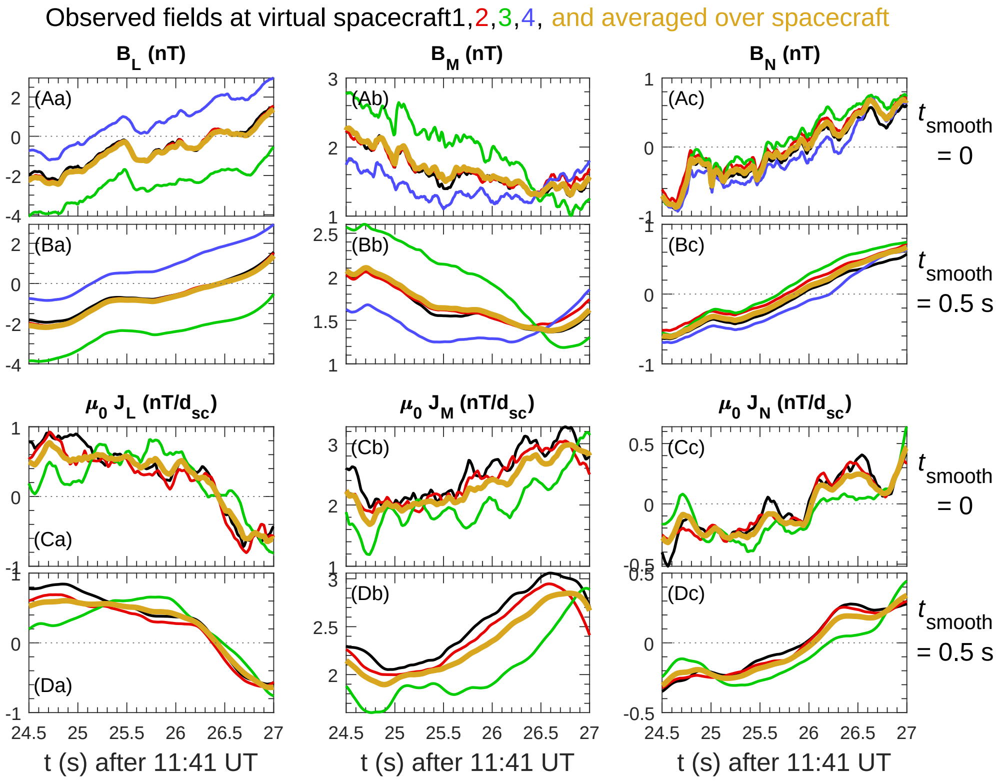

Figure 12. Input data to the reconstruction of data for MMS event on 27 August, 2018, showing the effects of the $t_{\mathrm{smooth}} = 0.5$ s smoothing used for the reconstruction. The (a) L, (b) M, and (c) N components of (A–B) the magnetic field $\mathbf{B}$, and (C–D) $\mu_0\mathbf{J}$ in units of nT/d_{sc}. (A and C) show the fields for the raw data without any smoothing, (B and D) show the fields with a boxcar smoothing time of $t_{\mathrm{smooth}} = 0.5$ s.

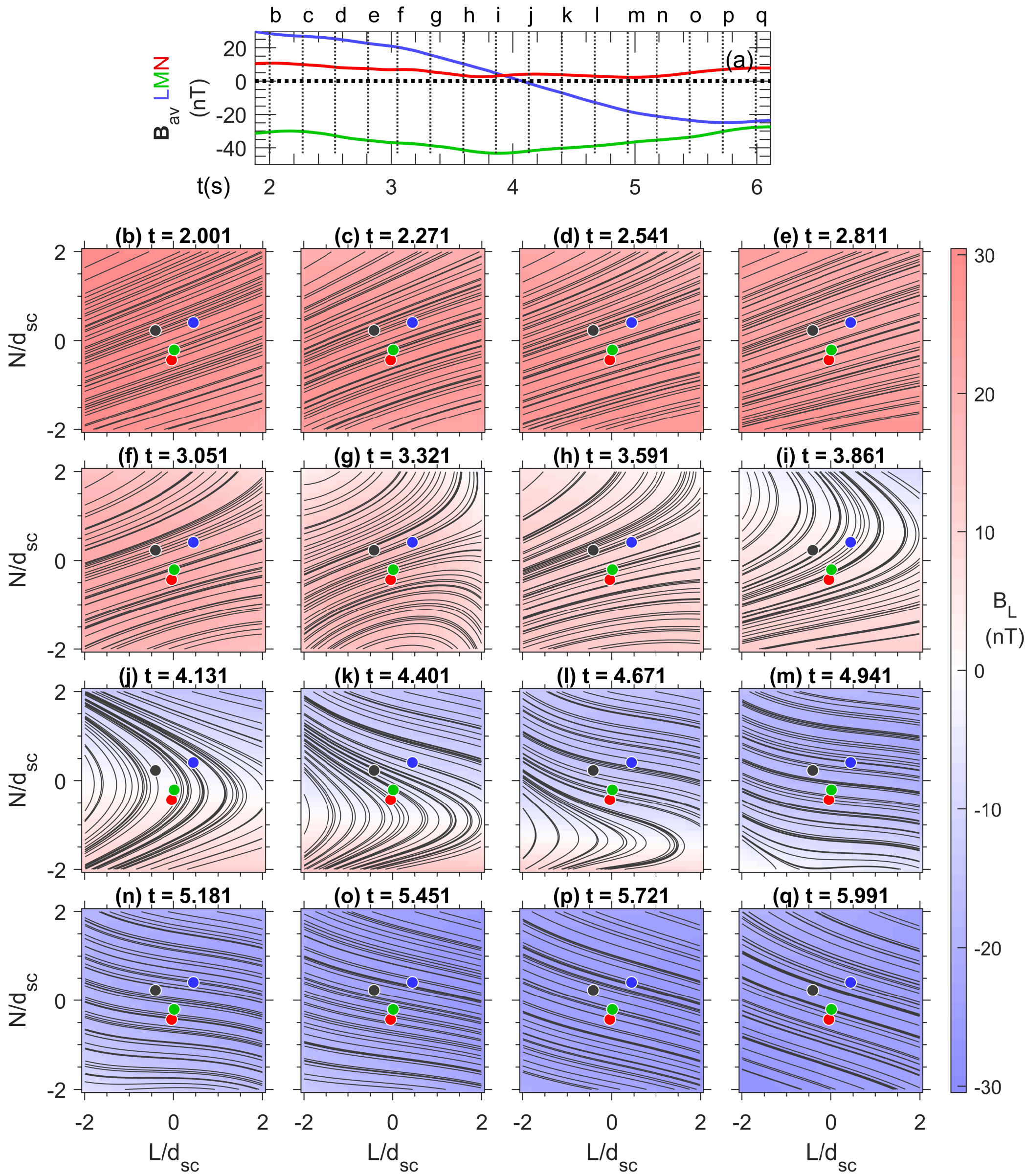

Figure 13. Reconstruction of the magnetic field for the magnetopause crossing event observed by MMS and described by Fuselier et al. (2019). This plot has the same format as Figure 5, except that the color shows B_L rather than B_M. The time is measured in s after 15:19 UT on 7 December, 2016.

The reconstruction yields average values of $v_L = -32$ km/s and $v_N = -19$ km/s. But although the direction of the neglected velocity component, $\mathbf{e}_m$, is usually closer to $\mathbf{e}_M$ than to $\mathbf{e}_L$ or $\mathbf{e}_N$, $\mathbf{e}_m$ always has a significant L component, which may lead to significant error in v_L.

There are some features in Figure 13 that are probably unrealistic, such as the downward curvature of the magnetic field in the L-N plane near the bottom of Figure 13g and the bumpiness of the magnetic field at the bottom edge of Figure 13m. But overall, Figures 13b–13q show consistent motion through a rotational discontinuity, as expected from the analysis of Fuselier et al. (2019).

5 Discussion

5.1 Test using simulation fields

We tested our reconstruction model using data from a simulation of magnetic reconnection (Liu et al., 2019). A key feature of our simulation data was that it was genuinely three-dimensional, as shown in Figure 1. Tests of reconstruction results using two-dimensional simulations benefit from the severe constraint of that assumption and may have much smaller errors.

We introduced a new variation of our polynomial reconstruction model that allows us to use multiple observation times as input. With the increased amount of data, we were able to use a complete quadratic expansion (CQ-3D model of equations(1)) and also get an estimate of the magnetic structure velocity (Figure 9), yielding values similar to those from the Spatio-Temporal Difference (STD) method (Shi et al., 2006, 2019).

But we also tested other variations of the reconstruction model with reduced sets of expansion terms (section 2 with Table 1). With a reduced number of expansion coefficients, we were able to test the single-time input method of Denton et al. (2020) and compare those results to those using multiple input times. In order to compare the results from different methods, we introduced a measure of the average vector difference between the simulation and reconstructed field, $d\underline{B}_{\mathrm{err,av}}$ (equation (6)), and listed values for this quantity in Table 2 at three different radii R from the centroid of the virtual spacecraft used to create input data for the reconstruction.

5.2 Effects of smoothing

Using the multiple-time input method, we first examined the effect of smoothing the input data (Figure 2). With a minimal amount of boxcar smoothing ($t_{\mathrm{smooth}} = 0.4$, case 1 in Table 2), the errors were small ($d\underline{B}_{\mathrm{err,av}} \sim 0.1$) close to the centroid of the spacecraft at $R = 0.35 d_{\mathrm{sc}}$ and 1 d_{sc}, but very large ($d\underline{B}_{\mathrm{err,av}} \sim 0.6$) farther away from the spacecraft at $R = 2 d_{\mathrm{sc}}$. In this case, many of the reconstructed magnetic field patterns were inconsistent with the simulation fields (Figure 5 and movie S1). With a moderate amount of smoothing ($t_{\mathrm{smooth}} = 0.8$, case 2 in Table 2), a substantial decrease in the errors at $R = 2 d_{\mathrm{sc}}$ was achieved ($d\underline{B}_{\mathrm{err,av}} \sim 0.33$ instead of 0.6) at the expense of a small increase in the errors at smaller R ($d\underline{B}_{\mathrm{err,av}} = 0.165$). And with $t_{\mathrm{smooth}} = 0.8$, the reconstructed fields were much more consistent with the simulation (Figure 4 and movie S3).

One can well question how one would know that reconstructed fields are reasonable for events observed in space. In that case, we are looking for several characteristics. First of all, the reconstructed fields should roughly match the observed fields at the spacecraft location, and the reconstructed field at the centroid of the spacecraft locations should be similar (though not necessarily exactly the same) to the field values averaged over the spacecraft (Figure 4). But this is a necessary, but not sufficient condition for validity of the reconstructions. The second thing we look for is for consistency of the reconstructions from one time to the next (like comparing the reconstructed magnetic field in the panels of Figure 5, Figure 6, or movies S1 and S3). Of course there may be some time variation in the magnetic structure (Denton et al., 2020), but we do not expect sudden changes in the large-scale structure of the magnetic field on very small timescales. Furthermore, we can see if the observed dynamics are reasonable. We don't normally expect, for instance, elongated islands to reconnect along their axis of elongation, because that would not be energetically favorable (would be working against the field line bending).

Using these considerations, we would probably consider the reconstructions with $t_{\mathrm{smooth}} = 0.8$ to be more realistic than those with $t_{\mathrm{smooth}} = 0.4$, even if we didn't know in advance what the reconstructed field should look like. But we must keep in mind that with smoothing of $t_{\mathrm{smooth}} = 0.8$ we will not be resolving changes in magnetic structure at smaller time scales.

5.3 Results for multiple input times versus single input times

Use of multiple input times over a time span $t_{\mathrm{input}} = 0.4$ resulted in somewhat smaller errors than the single-time input method ($t_{\mathrm{input}} = 0$), comparing $d\underline{B}_{\mathrm{err,av}}$ at $R = 2d_{\mathrm{sc}}$ for case 2 to that of case 5 in Table 2 (0.33 compared to 0.38 respectively). Errors for the single-time input Q-3D model (case 6 in Table 2) were much larger at $R = 2d_{\mathrm{sc}}$ ($d\underline{B}_{\mathrm{err,av}} = 0.55$), due to the problem of overfitting mentioned in section 2. Using the single-time input method, the smallest errors at $R = 2d_{\mathrm{sc}}$ were for the linear model LB-3D (case 4 in Table 2) (with $d\underline{B}_{\mathrm{err,av}} = 0.36$ compared to 0.38 for the RQ-3D model). This shows that the linear model is not a bad choice for determining, for instance, the position of an X line (Fu et al., 2015, 2016).

5.4 Results for different models

Based on the errors in Table 2, we are inclined to recommend the method of case 2 (same as case 8), which used the multiple-time input method with $t_{\mathrm{input}} = t_{\mathrm{smooth}}/2$, employed the RQ-3D model, and calculated a velocity with only components in the l and n directions. But in most of the cases, the variations in the errors were small. The only cases with very large errors were the ones already mentioned, small t_{smooth} and use of the Q-3D model with data from only a single observation time ($t_{\mathrm{input}} = 0$). The Q-3D model could yield reasonably good results using data from a span of time. The Q-3D model had slightly smaller $d\underline{B}_{\mathrm{err,av}}$ than the CQ-3D model ($d\underline{B}_{\mathrm{err,av}} = 0.15$ and 0.36 at $R = 1d_{\mathrm{sc}}$ and $R = 2d_{\mathrm{sc}}$ for case 9 in Table 2, compared to 0.16 and 0.4 for case 10, respectively), almost certainly because the $\partial^2 B_i/\partial m^2$ terms really should be small, as suggested by results shown by Denton et al. (2020). But even the CQ-3D model yielded fairly accurate reconstructions using multiple input times (Figure 7).

5.5 Velocity calculation

When we solved for all three components of structure velocity, $\mathbf{v}_{\mathrm{str}}$, including the m or M component (cases 11-14 in Table 2), the m component was sometimes wildly inaccurate for the lower order LB-3D and RQ-3D methods (cases 11 and 12 respectively), as indicated by enormous error bars for all three velocity components in Table 2. Using the higher order Q-3D and CQ-3D methods (cases 13 and 14 respectively), it was possible to solve for all three components of the structure velocity. And in that case, the calculated L component of the velocity ($v_{\mathrm{str},L}$ in Table 2) was slightly closer to the correct value of -3 than if the m or M component was not calculated (comparing $v_{\mathrm{str},L} = -2.6$ for case 13 versus -2.3 for case 9).

However, the M component of the calculated structure velocity was never close to the correct value of -2, no matter how we calculated it ($v_{\mathrm{str},M}$ in Table 2). This is yet another indication that the minimum gradient dependence cannot be accurately calculated when the minimum gradient is small (see results by Denton et al., 2021).

This suggests that one possible way to get a more accurate L component of $v_{\mathrm{str},L}$ would be to calculate a three-dimensional velocity, but then zero out the M component. The downside to that approach would be that the errors $dB_{\mathrm{err,av}}$ are somewhat larger for the high order Q-3D and CQ-3D methods than for the RQ-3D method (comparing cases 13 and 14 to case 8 in Table 2).

Using the median velocity components over the time modeled, all of the calculations of $v_{\mathrm{str},N}$ were reasonably close to the correct value of -1 (last column in Table 2). That again shows that the structure and inferred velocity are more accurate in the direction of the largest gradient.

5.6 Other variations of method

In the case of the simulation data, the M dependence was small (Figures 8b and 8h). A slight reduction in errors of the reconstructed fields was achieved by calculating the models in the L-M-N coordinates rather than the l-m-n coordinates (cases 15–18 and 22-24) and/or by dropping the m or M variation to get a 2D model (cases 19–24). But in order to make these simplifications, one would need to be very confident that the L-M-N coordinate system was optimal and that the structure really was approximately 2D.

Although we are inclined to recommend the RQ-3D model, the errors in Table 2 were only slightly worse for the linear LB-3D model (similar to the FOTE method of Fu et al. (2015, 2016)). The use of quadratic terms can sometimes lead to large first derivatives, whereas use of the linear equations severely constrains the solution. With linear equations, it would not be possible to reconstruct an X point and O point in the same field of view, as was found by Denton et al. (2020). And it's possible that there could be situations with large second derivatives. But if the third derivatives are large, none of these methods will be adequate.

5.7 Results for smoothed simulation data

Reconstruction cases 1–24 all compare the fields from the reconstruction using virtual spacecraft data that has been temporally smoothed to the unsmoothed simulation fields. This is useful for judging to what extent the reconstructed fields match the real fields around the spacecraft at one particular time. But perhaps the reconstruction would better describe simulation fields that have been smoothed in a similar way to the virtual spacecraft data. One could rotate the fields to orient them along the path of the spacecraft, and smooth in that direction. Here we approximate smoothing along that path by smoothing the simulation data with a boxcar average over 0.8 (d_i) in the N direction, 1.6 in the M direction, and 2.4 in the L direction. That is roughly consistent with our smoothing of the virtual spacecraft data with $t_{\mathrm{smooth}} = 0.8$ (equivalent to distance in the N direction) and our virtual spacecraft velocity of $(v_{\mathrm{sc},L}, v_{\mathrm{sc},M}, v_{\mathrm{sc},N}) = (3,2,1)$.

With this smoothing of the simulation data before calculating the error parameters, we find the results listed for cases 25–28 in Table 2, which are otherwise like cases 7–10. Calculated in this way, $dB_{\mathrm{err,av}}$ is much smaller, especially for the RQ-3D and Q-3D models. For case 26 (RQ-3D), $dB_{\mathrm{err,av}} = 0.062$, 0.075, and 0.31 at $R = 0.35 d_{\mathrm{sc}}$, $1 d_{\mathrm{sc}}$, and $2 d_{\mathrm{sc}}$, respectively. That is, the RQ-3D model does an excellent job modeling the smoothed simulation magnetic field within the spacecraft centroid and at a distance of $1 d_{\mathrm{sc}}$. The agreement is not as good at $2 d_{\mathrm{sc}}$, but appears to be about the best that we can get using our current polynomial reconstruction method.

5.8 Results for MMS events

In sections 4.1 and 4.2 we show reconstructions using our multiple-time input method with the RQ-3D model for two events observed by the MMS spacecraft. In the first case, our method reconstructs an X line very close to MMS1 (Figure 10), as was inferred from the spacecraft observations (Li et al., 2021). This event occurred on 27 August 2018 event, after the partial failure of the FPI instrument on MMS4, which occurred 7 June 2018. Our new version of the reconstruction code includes the capability of analyzing such events (see the acknowledgments section for a link to the code).

In order to show that we do not always see an X line in our reconstructions, we also showed a magnetopause crossing on 7 December 2016 for which there was a rotational discontinuity (Fuselier et al., 2019)

5.9 Conclusions and future directions

The models that we considered are based on a polynomial or Taylor expansion of the magnetic field, and are summarized in Table 1. Polynomial expansion is one tool for determining the structure of the magnetic field and its velocity relative to the spacecraft, but readers should keep in mind that Grad-Shafranov-type reconstruction (Hasegawa et al., 2019, and references therein) can be a complementary technique. Polynomial expansion has fewer assumptions and provides time-dependent variation, but Grad-Shafranov-type reconstruction has a larger set of data contributing to the calculation, which can be helpful for constraining the results.

We must do some smoothing of the input data in order to get physically reasonable results for the magnetic structure and its motion (section 3.3). With such smoothing, we are effectively modeling spatially smoothed fields, as can be seen by comparing $dB_{\mathrm{err,av}}$ for cases 25–28 (calculated using spatially smoothed fields) to those of cases 7-10 (calculated using the raw fields) in Table 2. So it should be kept in mind that the reconstructions using temporally smoothed input do not model the exact field at any one time, even within the spacecraft tetrahedron.

We have shown that our new method using multiple-time input results in some reduction in the error of the reconstructed fields, especially at large distances from the centroid of the spacecraft. This reduction is small for the LB-3D and RQ-3D models (comparing cases 7–8 to cases 4–5 in Table 2), but is quite large for the more complete Q-3D expansion (comparing case 9, with $dB_{\mathrm{err,av}} = 0.36$ at $R = 2d_{\mathrm{sc}}$ to case 6, with $dB_{\mathrm{err,av}} = 0.55$ at $R = 2d_{\mathrm{sc}}$). This makes sense because for single-time input, the Q-3D model had only one less parameter than the number of input quantities, so that overfitting was a big problem for that model.

One might think that with multiple-time input, we could use a cubic model. But the problem is that the spacecraft are moving approximately in a single direction during the time span of the input. So there's not enough information for a cubic model in the directions orthogonal to the spacecraft motion. One possible extension of this method is to expand in coordinates aligned with the spacecraft motion. Then a cubic or even more complex expansion could be used in that direction, and a quadratic expansion in the directions orthogonal to the spacecraft motion. As currently implemented, our estimate of the structure velocity from the reconstruction was not significantly better than that from the STD method Shi et al. (2006) (Figure 9). But we might be able to improve the velocity calculation using a higher order expansion along the spacecraft path, because that would allow us to use a significantly larger time span for input.

Currently our reconstruction code solves at all times for either just two components of the structure velocity (omitting the m or M component) or for all three components of the structure velocity. Another option would be to solve for all three components when

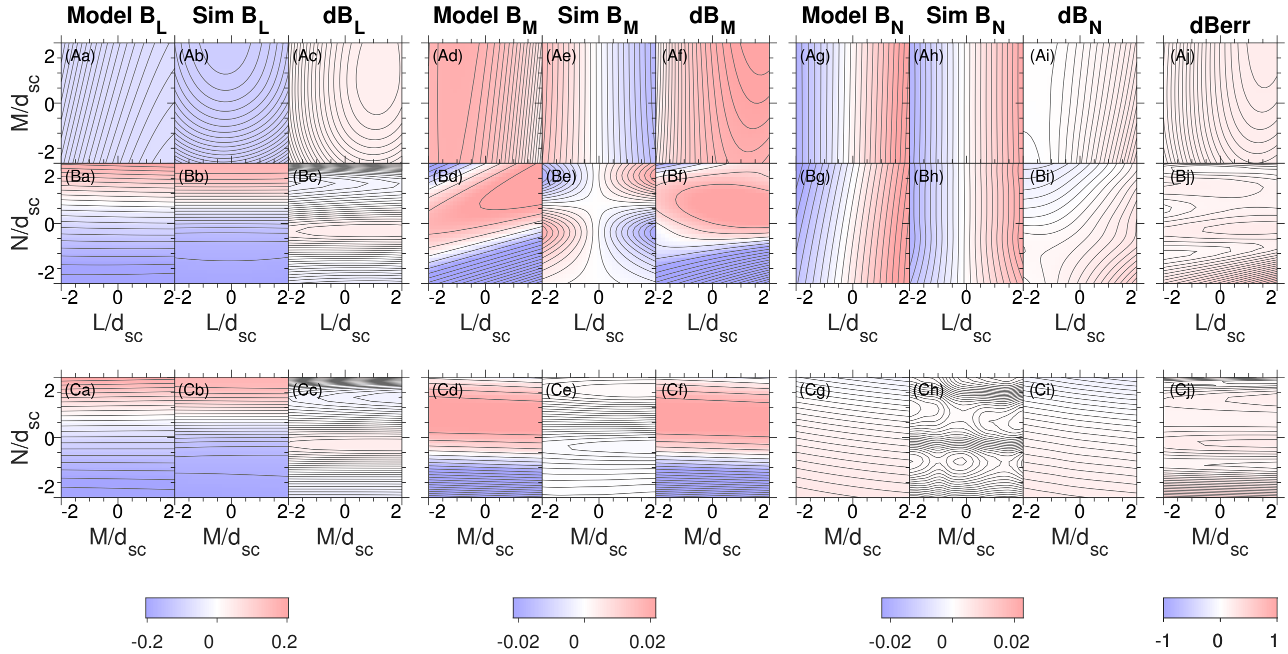

Figure 14. Two dimensional cuts of the model and simulation magnetic field, like in Figure 8, except for reconstruction case 3 in Table 2.

the minimum gradient eigenvalue is above a certain threshold. Another possible variation would be to assume that the velocity of the magnetic structure is more constant than we find using our new method or STD (Shi et al., 2006, 2019), and use a fixed velocity based on averaging STD or the reconstruction velocity over an interval of time.

While our reconstruction technique can yield useful visualizations of the magnetic structure, our comparison to simulation data shows that there can be substantial differences between the simulation and model fields (Figure 8). This means that one should be very careful when interpreting and using detailed features of reconstructed fields, like to trace particles. Some unrealistic features can be improved with more smoothing. Figure 14 is like Figure 8, except now for case 3 in Table 2 with $t_{\rm smooth} = 1.6$. Note that Figure 14Bh is much closer to Figure 14Bg than is Figure 8Bh to Figure 8Bg. The downsides to more smoothing are that effectively more spatially smoothed fields are being represented (subsection 5.7) and more time dependent behavior is excluded.

A model with fewer parameters is less likely to produce wild unphysical oscillations in the reconstructed fields. If one is inclined to use a more complete quadratic expansion, our results indicate that results are improved by dropping the $\partial^2 B_i/\partial m^2$ terms, that is, by using the Q-3D model rather than the CQ-3D model (comparing $dB_{\rm err,av}$ values for case 9 or 27 to those of case 10 or 28 in Table 2). A further reduction in the errors is achieved by using the RQ-3D model (comparing $dB_{\rm err,av}$ values for case 8 or 26 to those of case 9 or 27 in Table 2). For instance, at $R = 2d_{\rm sc}$ outside the spacecraft tetrahedron, the reconstructed fields from the RQ-3D model had $dB_{\rm err,av}$ calculated using the spatially smoothed fields equal to $dB_{\rm err,av} = 0.31$ whereas $dB_{\rm err,av}$ for the Q-3D model was 0.35. The linear LB-3D model is even less likely to produce wild oscillations, since it can only represent linear gradients, and could be useful for some purposes. But the RQ-3D model had smaller errors than the linear LB-3D model, suggesting perhaps that the RQ-3D model is often optimal.

6 Open Research Data Availability

The new version of our Matlab reconstruction code, IDL programs for downloading the MMS data, and instructions for running them are available in a Zenodo repository at doi:10.5281/zenodo.6395045, along with data from the particle in cell simulation and a draft of the paper and Supplementary Information. The Supplementary Information includes plots like Figure 6 and movies showing the reconstructions in the L-N and M-N planes for simulation reconstruction cases 1 and 7–10. Movies are also included for the two MMS events. All MMS data are available on-line at https://lasp.colorado.edu/mms/sdc/public

Appendix A Model equations for $\boldsymbol{\mu_0}\mathbf{J}$ and $\nabla \cdot \mathbf{B}$

Taking the curl of equations (1), the equations for $\mu_0\mathbf{J}$ for the CQ-3D model are

$$\begin{aligned}
\mu_0 J_L &= \frac{\partial B_N}{\partial M} + \frac{\partial^2 B_N}{\partial L \partial M} L + \frac{\partial^2 B_N}{\partial M^2} M + \frac{\partial^2 B_N}{\partial M \partial N} N \\
&\quad - \left(\frac{\partial B_M}{\partial N} + \frac{\partial^2 B_M}{\partial L \partial N} L + \frac{\partial^2 B_M}{\partial M \partial N} M + \frac{\partial^2 B_M}{\partial N^2} N \right), \qquad \text{(A1)} \\
\mu_0 J_M &= \frac{\partial B_L}{\partial N} + \frac{\partial^2 B_L}{\partial L \partial N} L + \frac{\partial^2 B_L}{\partial M \partial N} M + \frac{\partial^2 B_L}{\partial N^2} N \\
&\quad - \left(\frac{\partial B_N}{\partial L} + \frac{\partial^2 B_N}{\partial L^2} L + \frac{\partial^2 B_N}{\partial L \partial M} M + \frac{\partial^2 B_N}{\partial L \partial N} N \right), \qquad \text{(A2)} \\
\mu_0 J_N &= \frac{\partial B_M}{\partial L} + \frac{\partial^2 B_M}{\partial L^2} L + \frac{\partial^2 B_M}{\partial L \partial M} M + \frac{\partial^2 B_M}{\partial L \partial N} N \\
&\quad - \left(\frac{\partial B_L}{\partial M} + \frac{\partial^2 B_L}{\partial L \partial M} L + \frac{\partial^2 B_L}{\partial M^2} M + \frac{\partial^2 B_L}{\partial M \partial N} N \right). \qquad \text{(A3)}
\end{aligned}$$

The reduced models are usually expressed in terms of l, m, and n rather than L, M, and N, and derivatives neglected in the reduced models (Table 1) would not be included in the calculation of $\mu_0\mathbf{J}$. For instance, the Q-3D model does not include terms with $\partial^2/\partial m^2$.

Taking the divergence of equations (1), we get the following four equations.

$$\begin{aligned}
0 &= \frac{\partial B_L}{\partial L} + \frac{\partial B_M}{\partial M} + \frac{\partial B_N}{\partial N}, \qquad \text{(A4)} \\
0 &= \frac{\partial^2 B_L}{\partial L^2} + \frac{\partial^2 B_M}{\partial L \partial M} + \frac{\partial^2 B_N}{\partial L \partial N}, \qquad \text{(A5)} \\
0 &= \frac{\partial^2 B_L}{\partial L \partial M} + \frac{\partial^2 B_M}{\partial M^2} + \frac{\partial^2 B_N}{\partial M \partial N}, \qquad \text{(A6)} \\
0 &= \frac{\partial^2 B_L}{\partial L \partial N} + \frac{\partial^2 B_M}{\partial M \partial N} + \frac{\partial^2 B_N}{\partial N^2}, \qquad \text{(A7)}
\end{aligned}$$

where equations (A5), (A6), and (A7) have been divided respectively by L, M, and N. Only (A4) is useful for the LB-3D and RQ-3D models, since all the terms in the other equations are neglected.

Acknowledgments

RED was supported by NASA grant 80NSSC19K0254. HH was supported by JSPS Grant-in-aid for Scientific Research KAKENHI 21K03504. We thank all the members of the MMS Science Working Team for their many contributions to this work.

References

Denton, R. E., Sonnerup, B. U. O., Hasegawa, H., Phan, T. D., Russell, C. T., Strangeway, R. J., ... Torbert, R. B. (2016). Motion of the MMS spacecraft relative to the magnetic reconnection structure observed on 16 October 2015 at 1307 UT. *Geophys. Res. Lett.*, *43*(11), 5589–5596. doi: 10.1002/2016gl069214

Denton, R. E., Sonnerup, B. U. O., Russell, C. T., Hasegawa, H., Phan, T. D., Strangeway, R. J., ... Vines, S. K. (2018). Determining L-M-N Current Sheet Coordinates at the Magnetopause From Magnetospheric Multiscale Data. *J. Geophys. Res.*, *123*(3), 2274–2295. doi: 10.1002/2017ja024619

Denton, R. E., Torbert, R. B., Hasegawa, H., Dors, I., Genestreti, K. J., Argall, M. R., ... Fischer, D. (2020, February). Polynomial reconstruction of the reconnection magnetic field observed by multiple spacecraft. *JOURNAL OF GEOPHYSICAL RESEARCH-SPACE PHYSICS*, *125*(2). (tex.article-number: e2019JA027481 tex.eissn: 2169-9402 tex.orcid-numbers: Hasegawa, Hiroshi/0000-0002-1172-021X tex.researcherid-numbers: MMS, Science Team NASA/J-5393-2013 Hasegawa, Hiroshi/A-1192-2007 tex.unique-id: ISI:000535395800016) doi: 10.1029/2019JA027481

Denton, R. E., Torbert, R. B., Hasegawa, H., Manuzzo, R., Belmont, G., Rezeau, L., ... Giles, B. L. (2021). Two-dimensional velocity of the magnetic structure observed on 11 July 2017 by the Magnetospheric Multiscale spacecraft. *Journal of Geophysical Research-Space Physics*, *126*. doi: 10.1029/2020JA028705

Fu, H. S., Cao, J. B., Vaivads, A., Khotyaintsev, Y. V., Andre, M., Dunlop, M., ... Eriksson, E. (2016, February). Identifying magnetic reconnection events using the FOTE method. *JOURNAL OF GEOPHYSICAL RESEARCH-SPACE PHYSICS*, *121*(2), 1263–1272. (tex.eissn: 2169-9402 tex.orcid-numbers: Khotyaintsev, Yuri/0000-0001-5550-3113 Fu, Huishan/0000-0002-4701-7219 Vaivads, Andris/0000-0003-1654-841X Liu, Wenlong/0000-0001-7991-5067 dunlop, malcolm w/0000-0002-8195-5137 Liu, Wenlong/0000-0001-7991-5067 tex.researcherid-numbers: Khotyaintsev, Yuri/AAX-9720-2021 Fu, Huishan/E-1507-2012 Vaivads, Andris/H-8169-2013 Liu, Wenlong/Y-7669-2019 dunlop, malcolm w/F-1347-2010 Liu, Wenlong/G-5585-2013 tex.unique-id: WOS:000373002100023) doi: 10.1002/2015JA021701

Fu, H. S., Vaivads, A., Khotyaintsev, Y. V., Olshevsky, V., Andre, M., Cao, J. B., ... Lapenta, G. (2015, May). How to find magnetic nulls and reconstruct field topology with MMS data? *JOURNAL OF GEOPHYSICAL RESEARCH-SPACE PHYSICS*, *120*(5), 3758–3782. (tex.eissn: 2169-9402 tex.orcid-numbers: Fu, Huishan/0000-0002-4701-7219 Khotyaintsev, Yuri/0000-0001-5550-3113 Vaivads, Andris/0000-0003-1654-841X Retino, Alessandro/0000-0001-5824-2852 Lapenta, Giovanni/0000-0002-3123-4024 tex.researcherid-numbers: Fu, Huishan/E-1507-2012 Khotyaintsev, Yuri/AAX-9720-2021 Vaivads, Andris/H-8169-2013 Lapenta, Giovanni/J-5221-2016 tex.unique-id: WOS:000357869600035) doi: 10.1002/2015JA021082

Fu, H. S., Wang, Z., Zong, Q., Chen, X. H., He, J. S., Vaivads, A., & Olshevsky, V. (2020). Methods for finding magnetic nulls and reconstructing field topology: A review. In Zong, Q and Escoubet, P and Sibeck, D and Le, G and Zhang, H (Ed.), *DAYSIDE MAGNETOSPHERE INTERACTIONS* (Vol. 248, pp. 153–172). (ISSN: 0065-8448 tex.orcid-numbers: Fu, Huishan/0000-0002-4701-7219 Zong, Qiugang/0000-0002-6414-3794 tex.researcherid-numbers: Fu, Huishan/E-1507-2012 Zong, Qiugang/L-1920-2018 tex.unique-id: WOS:000637603000010)

Fuselier, S. A., Trattner, K. J., Petrinec, S. M., Pritchard, K. R., Burch, J. L., Cassak, P. A., ... Strangeway, R. J. (2019, November). Stationarity of the reconnection x-line at earth's magnetopause for southward IMF. *JOURNAL OF GEOPHYSICAL RESEARCH-SPACE PHYSICS*, *124*(11), 8524–8534. (tex.earlyaccessdate: NOV 2019 tex.eissn: 2169-9402 tex.orcid-numbers: Giles, Barbara L/0000-0001-8054-825X Strangeway, Robert/0000-0001-9839-1828 Fuselier, Stephen/0000-0003-4101-7901 Burch, James/0000-0003-0452-8403 Pritchard, Kristina/0000-0002-6523-6263 TRATTNER, KARLHEINZ/0000-0001-5169-109X tex.researcherid-numbers: Giles, Barbara L/J-7393-2017 tex.unique-id: WOS:000494920500001) doi: 10.1029/2019JA027143

Gershman, D. J., Avanov, L. A., Boardsen, S. A., Dorelli, J. C., Gliese, U., Barrie, A. C., … Pollock, C. J. (2017, November). Spacecraft and instrument photoelectrons measured by the dual electron spectrometers on MMS. *JOURNAL OF GEOPHYSICAL RESEARCH-SPACE PHYSICS*, *122*(11), 11548–11558. (tex.eissn: 2169-9402 tex.orcid-numbers: Giles, Barbara L/0000-0001-8054-825X Avanov, Levon/0000-0003-2357-4851 tex.researcherid-numbers: Giles, Barbara L/J-7393-2017 tex.unique-id: WOS:000419938600040) doi: 10.1002/2017JA024518

Haaland, S., Runov, A., Artemyev, A., & Angelopoulos, V. (2019, May). Characteristics of the flank magnetopause: THEMIS observations. *JOURNAL OF GEOPHYSICAL RESEARCH-SPACE PHYSICS*, *124*(5), 3421–3435. (tex.eissn: 2169-9402 tex.researcherid-numbers: Artemyev, Anton/AAO-8011-2020 tex.unique-id: WOS:000471601500019) doi: 10.1029/2019JA026459

Hasegawa, H., Denton, R. E., Nakamura, R., Genestreti, K. J., Nakamura, T. K. M., Hwang, K. J., … Saito, Y. (2019). Reconstruction of the Electron Diffusion Region of Magnetotail Reconnection seen by the MMS Spacecraft on 11 July 2017. *J. Geophys. Res.*, *124*(1), 122–138. doi: 10.1029/2018ja026051

Korovinskiy, D. B., Kiehas, S. A., Panov, E. V., Semenov, V. S., Erkaev, N. V., Divin, A. V., & Kubyshkin, I. V. (2021, May). The Inertia-Based Model for Reconstruction of the Electron Diffusion Region. *Journal of Geophysical Research-Space Physics*, *126*(5), e2020JA029045. (WOS:000657463000045) doi: 10.1029/2020JA029045

Li, W.-Y., Khotyaintsev, Y., V, Tang, B.-B., Graham, D. B., Norgren, C., Vaivads, A., … Wang, C. (2021, August). Upper-hybrid waves driven by meandering electrons around magnetic reconnection x line. *GEOPHYSICAL RESEARCH LETTERS*, *48*(16). (tex.article-number: e2021GL093164 tex.eissn: 1944-8007 tex.orcid-numbers: Khotyaintsev, Yuri/0000-0001-5550-3113 Lindqvist, Per-Arne/0000-0001-5617-9765 Norgren, Cecilia/0000-0002-6561-2337 Dokgo, Kyunghwan/0000-0003-3917-7885 Tang, BINBIN/0000-0002-9244-1828 Graham, Daniel/0000-0002-1046-746X Andre, Mats/0000-0003-3725-4920 tex.researcherid-numbers: Khotyaintsev, Yuri/AAX-9720-2021 Lindqvist, Per-Arne/G-1221-2016 tex.unique-id: WOS:000688759800030) doi: 10.1029/2021GL093164

Liu, Y.-H., Li, T. C., Hesse, M., Sun, W. J., Liu, J., Burch, J., … Huang, K. (2019, April). Three-dimensional magnetic reconnection with a spatially confined x-line extent: Implications for dipolarizing flux bundles and the dawn-dusk asymmetry. *JOURNAL OF GEOPHYSICAL RESEARCH-SPACE PHYSICS*, *124*(4), 2819–2830. (tex.eissn: 2169-9402 tex.orcid-numbers: Sun, Wei-Jie/0000-0001-5260-658X Li, Tak Chu/0000-0002-6367-1886 Liu, Jiang/0000-0002-7489-9384 Burch, James/0000-0003-0452-8403 tex.researcherid-numbers: Sun, Wei-Jie/E-8097-2012 Liu, Jiang/B-3015-2014 tex.unique-id: ISI:000477707800034) doi: 10.1029/2019JA026539

Manuzzo, R., Belmont, G., Rezeau, L., Califano, F., & Denton, R. E. (2019, December). Crossing of Plasma Structures by Spacecraft: A Path Calculator. *JOURNAL OF GEOPHYSICAL RESEARCH-SPACE PHYSICS*, *124*(12), 10119–10140. doi: 10.1029/2019JA026632

Shi, Q. Q., Pu, Z. Y., Zhang, H., Fu, S. Y., Xiao, C. J., Zong, Q. G., … Liu, Z. X. (2005). Simulation studies of high-latitude magnetospheric boundary dynamics. *Surveys in Geophysics*, *26*(1-3), 369–386. doi: 10.1007/s10712-005-1900-6

Shi, Q. Q., Shen, C., Dunlop, M. W., Pu, Z. Y., Zong, Q. G., Liu, Z. X., … Balogh,

A. (2006). Motion of observed structures calculated from multi-point magnetic field measurements: Application to Cluster. *Geophys. Res. Lett.*, *33*(8). doi: 10.1029/2005gl025073

Shi, Q. Q., Tian, A. M., Bai, S. C., Hasegawa, H., Degeling, A. W., Pu, Z. Y., ... Liu, Z. Q. (2019). Dimensionality, Coordinate System and Reference Frame for Analysis of In-Situ Space Plasma and Field Data. *Space Science Reviews*, *215*(4). doi: 10.1007/s11214-019-0601-2

Sonnerup, B. U. O., Hasegawa, H., Teh, W. L., & Hau, L. N. (2006). Grad-Shafranov reconstruction: An overview. *J. Geophys. Res.*, *111*(A9). doi: 10.1029/2006JA011717

Sonnerup, B. U. O., & Teh, W.-L. (2008). Reconstruction of two-dimensional coherent MHD structures in a space plasma: The theory. *J. Geophys. Res.*, *113*(A5). doi: 10.1029/2007ja012718

Sonnerup, B. U. O., & Teh, W. L. (2009). Reconstruction of two-dimensional coherent structures in ideal and resistive Hall MHD: The theory. *J. Geophys. Res.*, *114*. doi: 10.1029/2008JA013897

Torbert, R. B., Dors, I., Argall, M. R., Genestreti, K. J., Burch, J. L., Farrugia, C. J., ... Strangeway, R. J. (2020, February). A New Method of 3-D Magnetic Field Reconstruction. *Geophysical Research Letters*, *47*(3), e2019GL085542. (WOS:000529107400048) doi: 10.1029/2019GL085542

Figure 1.

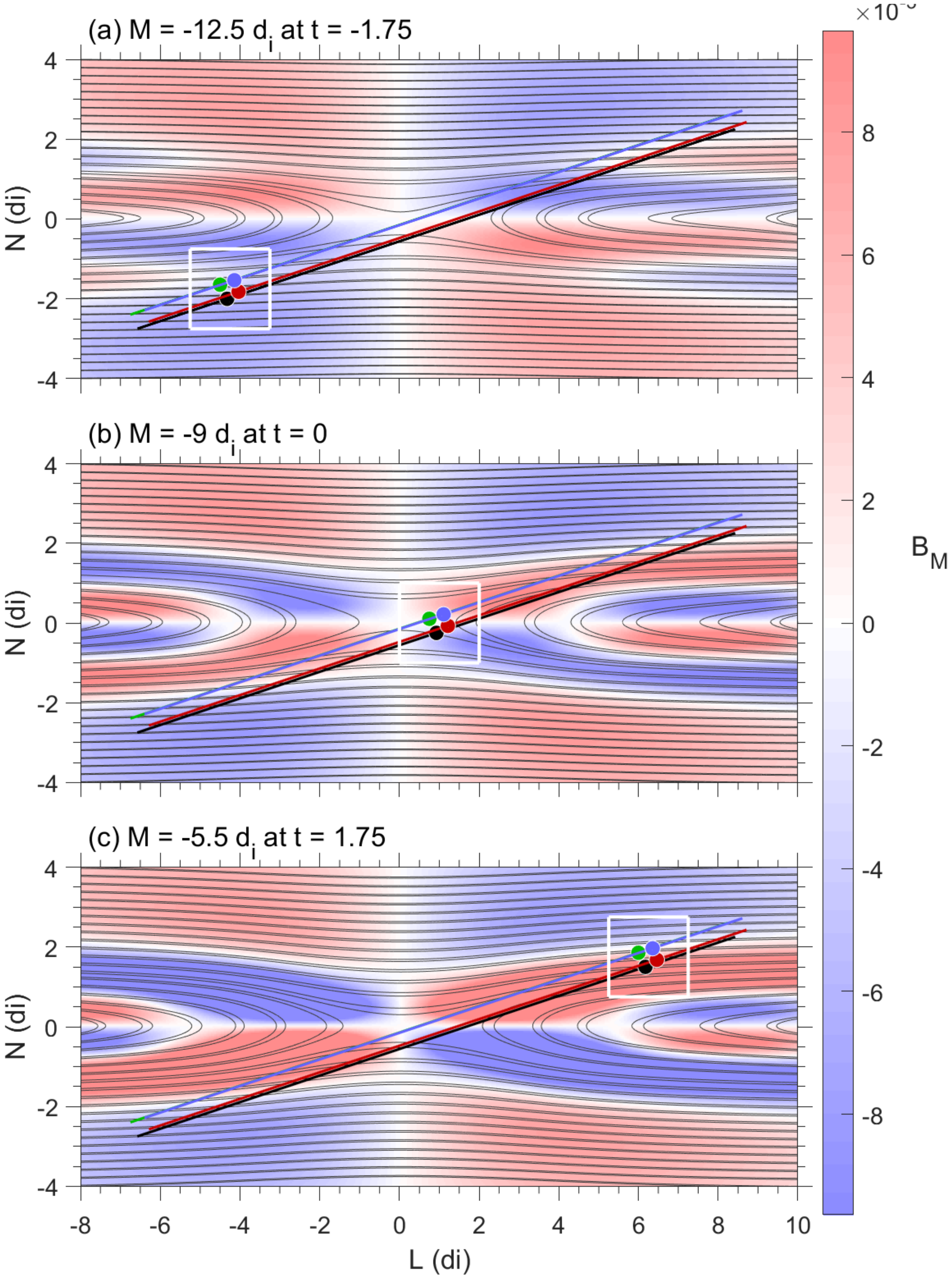
(a) M = -12.5 d_i at t = -1.75
(b) M = -9 d_i at t = 0
(c) M = -5.5 d_i at t = 1.75
N (di)
L (di)
B_M
×10^-3

Figure 2.

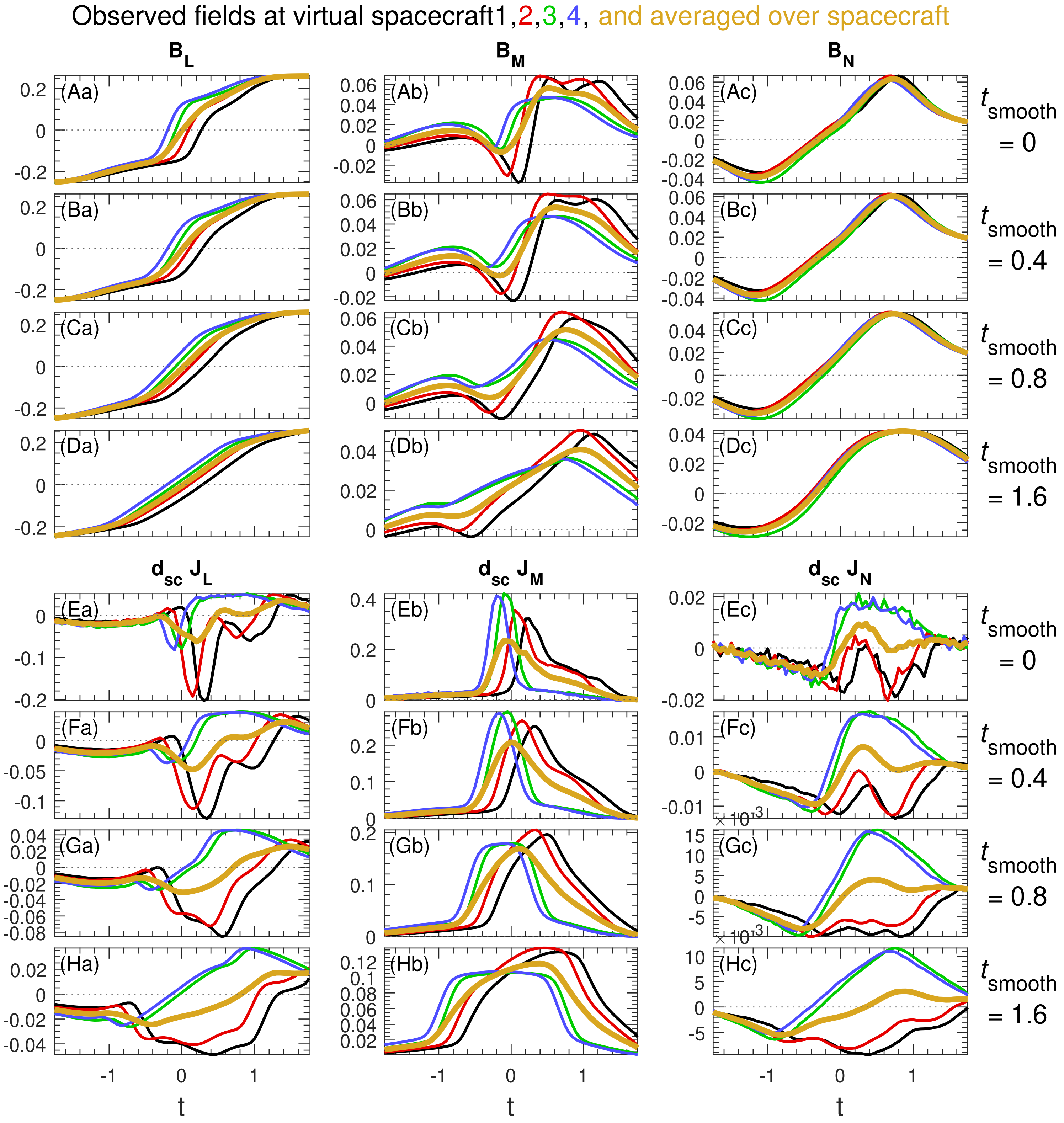

Observed fields at virtual spacecraft1,2,3,4, and averaged over spacecraft
B_L
B_M
B_N
d_{sc} J_L
d_{sc} J_M
d_{sc} J_N
t_{smooth} = 0
t_{smooth} = 0.4
t_{smooth} = 0.8
t_{smooth} = 1.6
(Aa) (Ab) (Ac) (Ba) (Bb) (Bc) (Ca) (Cb) (Cc) (Da) (Db) (Dc)
(Ea) (Eb) (Ec) (Fa) (Fb) (Fc) (Ga) (Gb) (Gc) (Ha) (Hb) (Hc)
t

Figure 3.

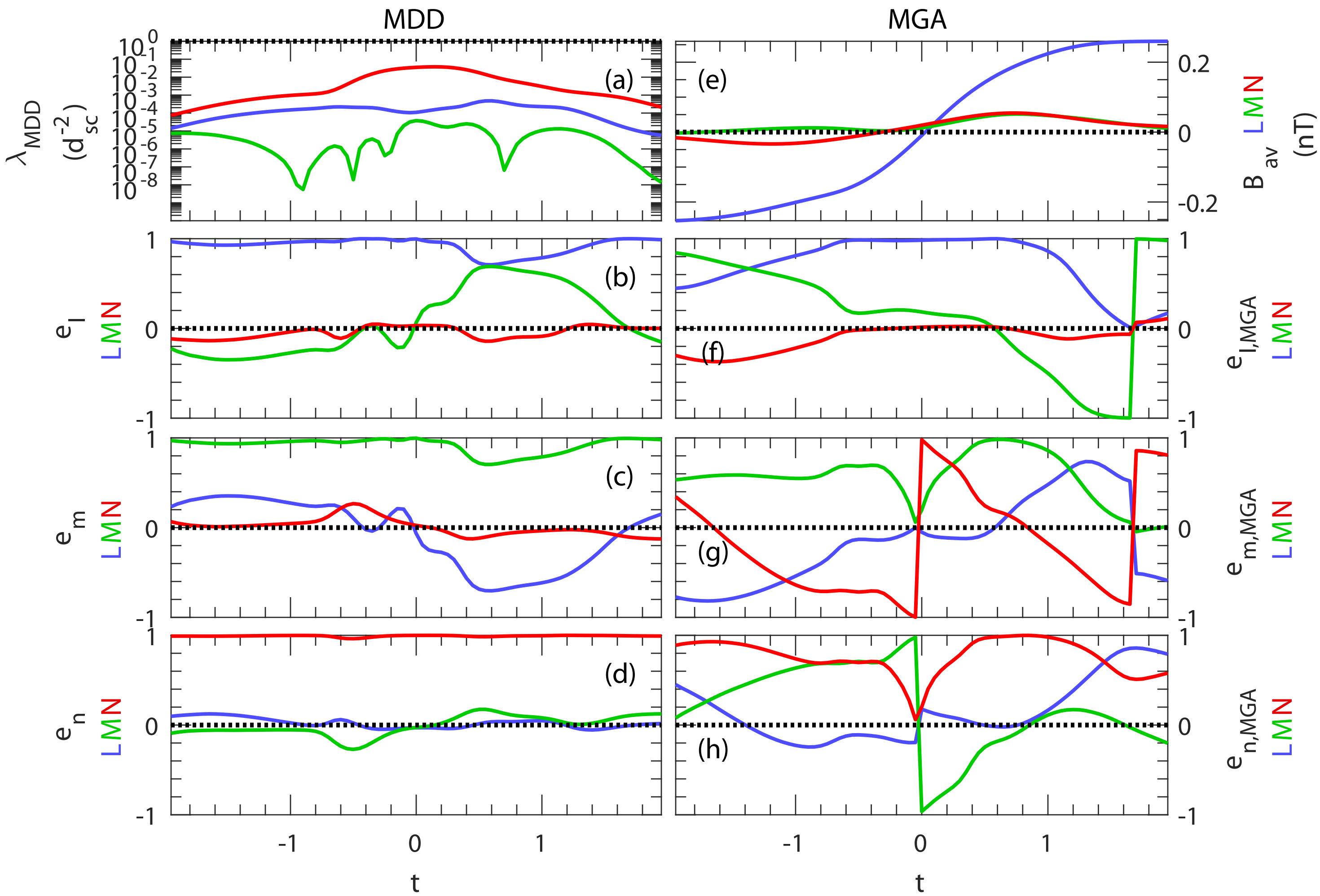

MDD
MGA
λ_{MDD} (d_{sc}^{-2})
(a)
(b)
(c)
(d)
(e)
(f)
(g)
(h)
e_l LMN
e_m LMN
e_n LMN
B_{av} LMN (nT)
$e_{l,MGA}$ LMN
$e_{m,MGA}$ LMN
$e_{n,MGA}$ LMN
t

Figure 4.

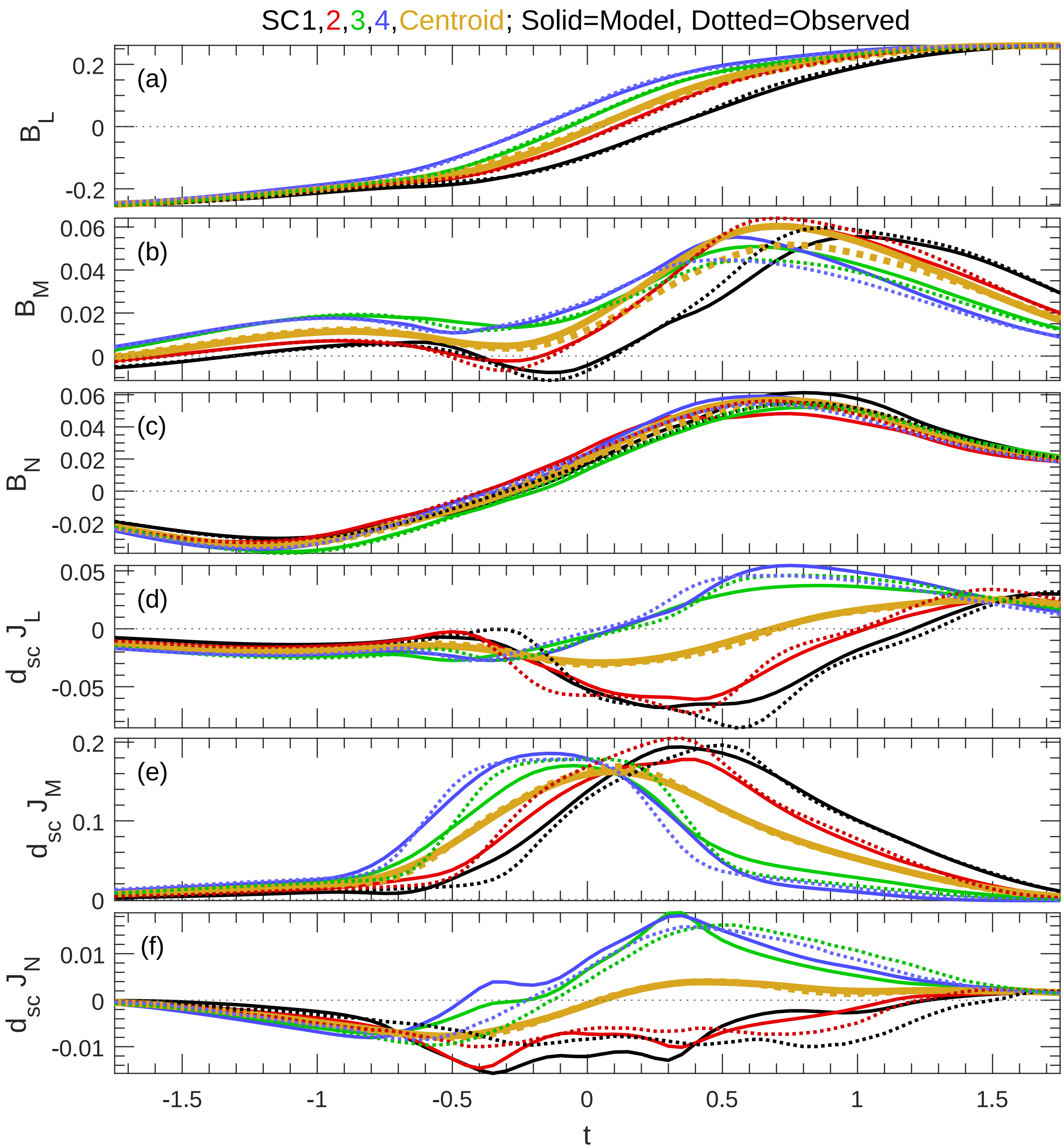
SC1,2,3,4,Centroid; Solid=Model, Dotted=Observed
(a)
(b)
(c)
(d)
(e)
(f)
B_L
B_M
B_N
d_sc J_L
d_sc J_M
d_sc J_N
t

Figure 5.

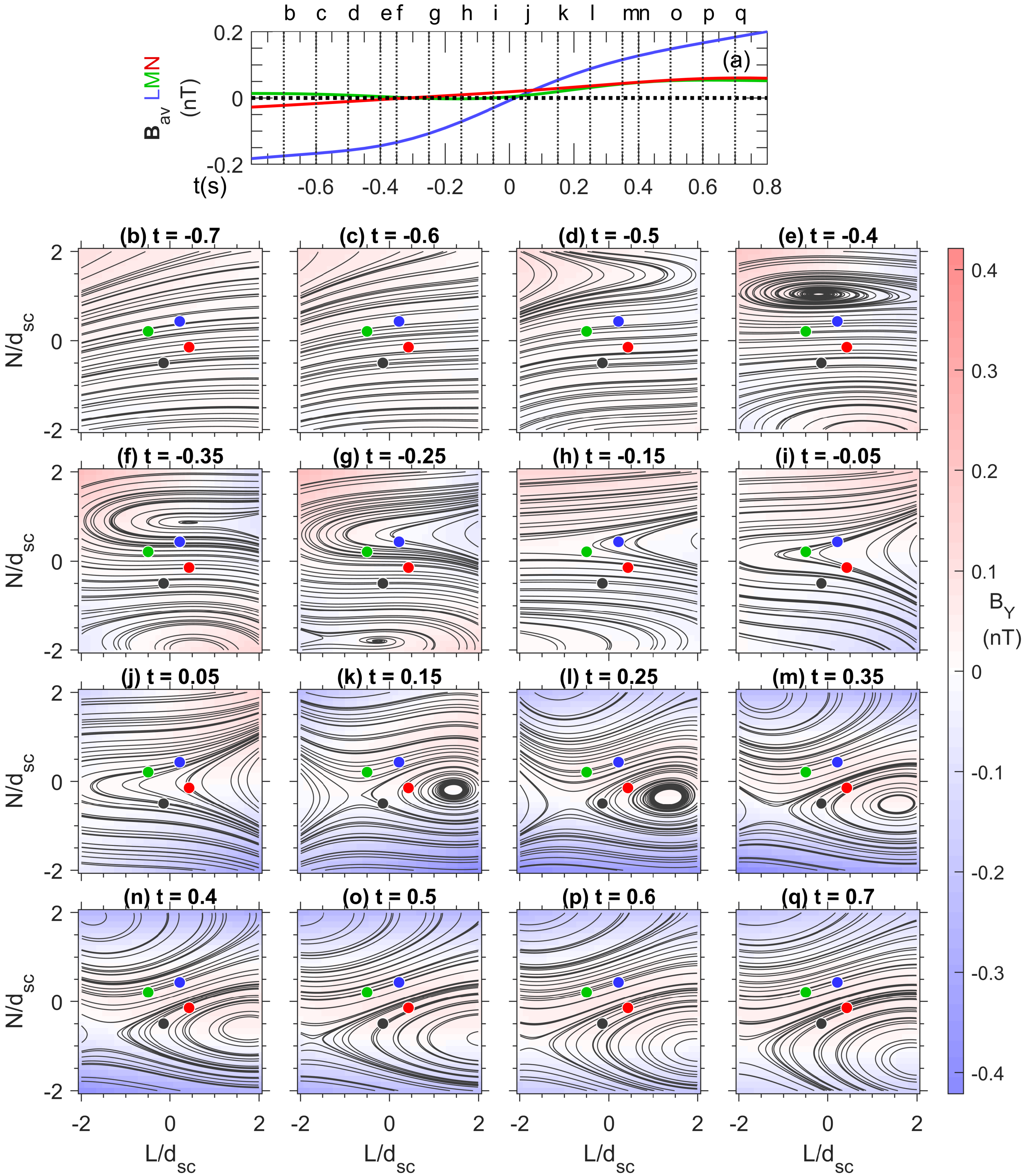

b c d e f g h i j k l m n o p q
(a)
B_{av} LMN (nT)
t(s)
(b) t = -0.7
(c) t = -0.6
(d) t = -0.5
(e) t = -0.4
(f) t = -0.35
(g) t = -0.25
(h) t = -0.15
(i) t = -0.05
(j) t = 0.05
(k) t = 0.15
(l) t = 0.25
(m) t = 0.35
(n) t = 0.4
(o) t = 0.5
(p) t = 0.6
(q) t = 0.7
N/d_{sc}
L/d_{sc}
B_Y (nT)

Figure 6.

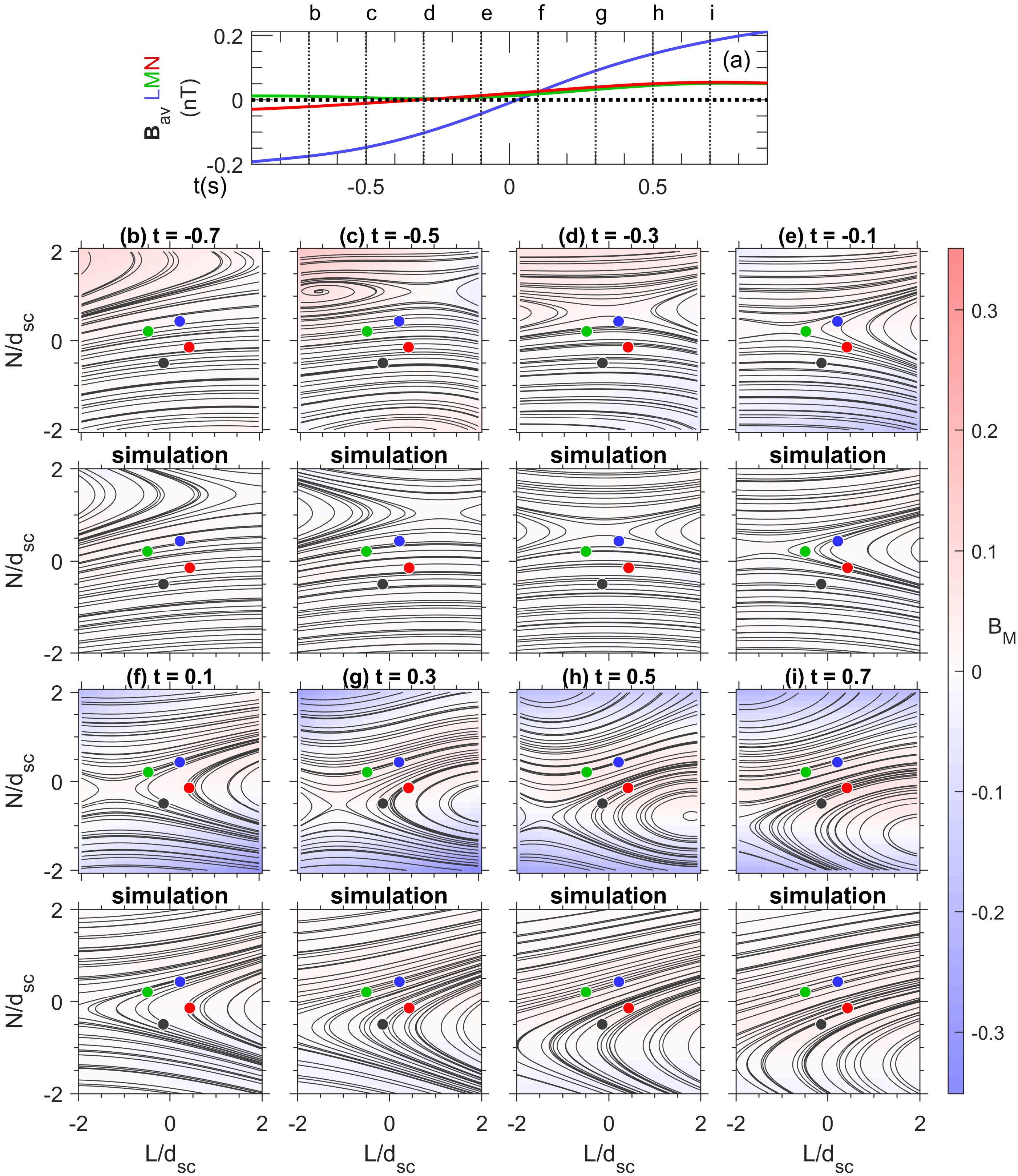

(a)
B_{av} LMN (nT)
t(s)
b c d e f g h i
(b) t = -0.7
(c) t = -0.5
(d) t = -0.3
(e) t = -0.1
(f) t = 0.1
(g) t = 0.3
(h) t = 0.5
(i) t = 0.7
simulation
N/d_{sc}
L/d_{sc}
B_M

Figure 7.

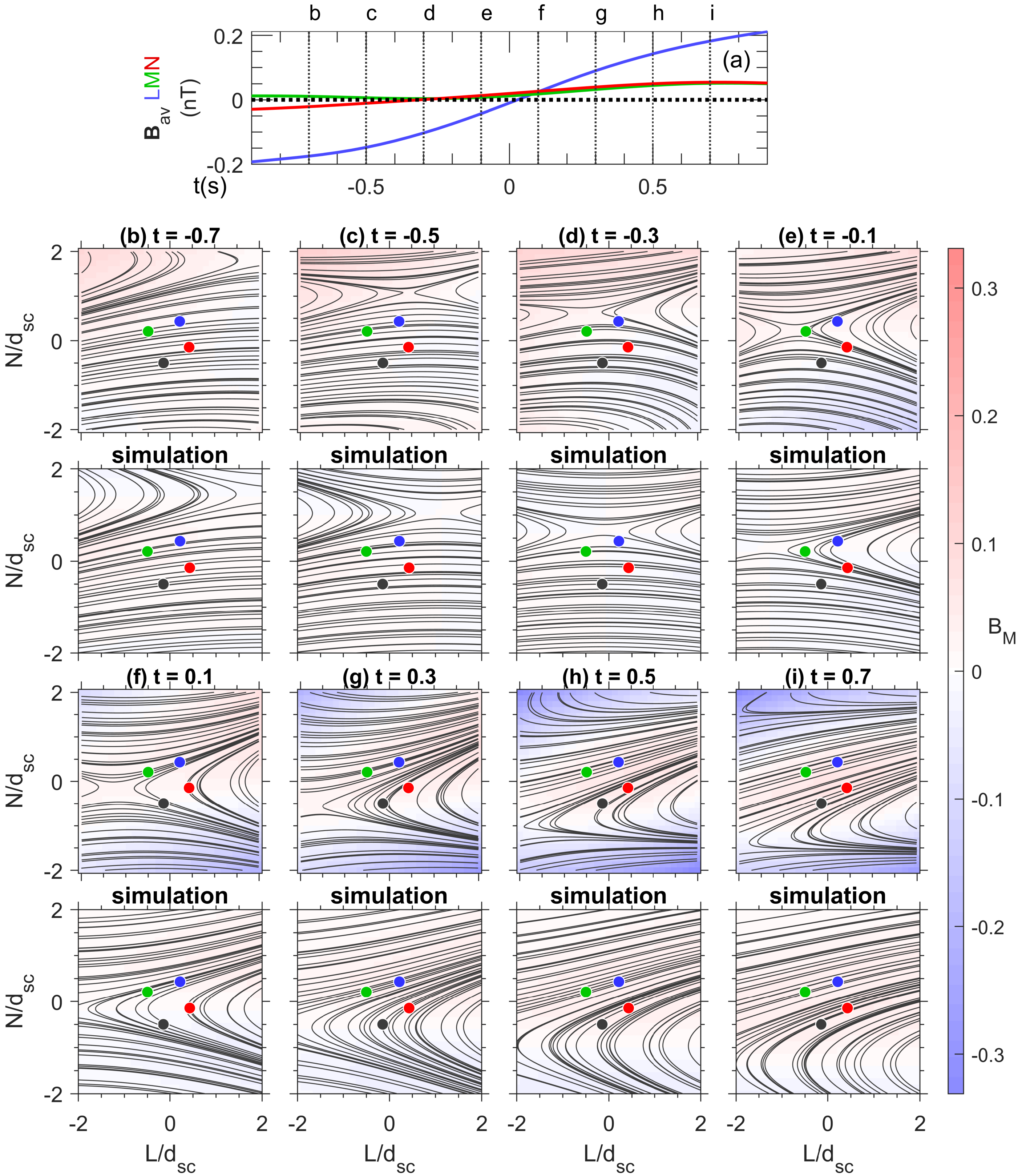

b
c
d
e
f
g
h
i
(a)
B_{av} LMN (nT)
t(s)
(b) t = -0.7
(c) t = -0.5
(d) t = -0.3
(e) t = -0.1
simulation
(f) t = 0.1
(g) t = 0.3
(h) t = 0.5
(i) t = 0.7
N/d_{sc}
L/d_{sc}
B_M

Figure 8.

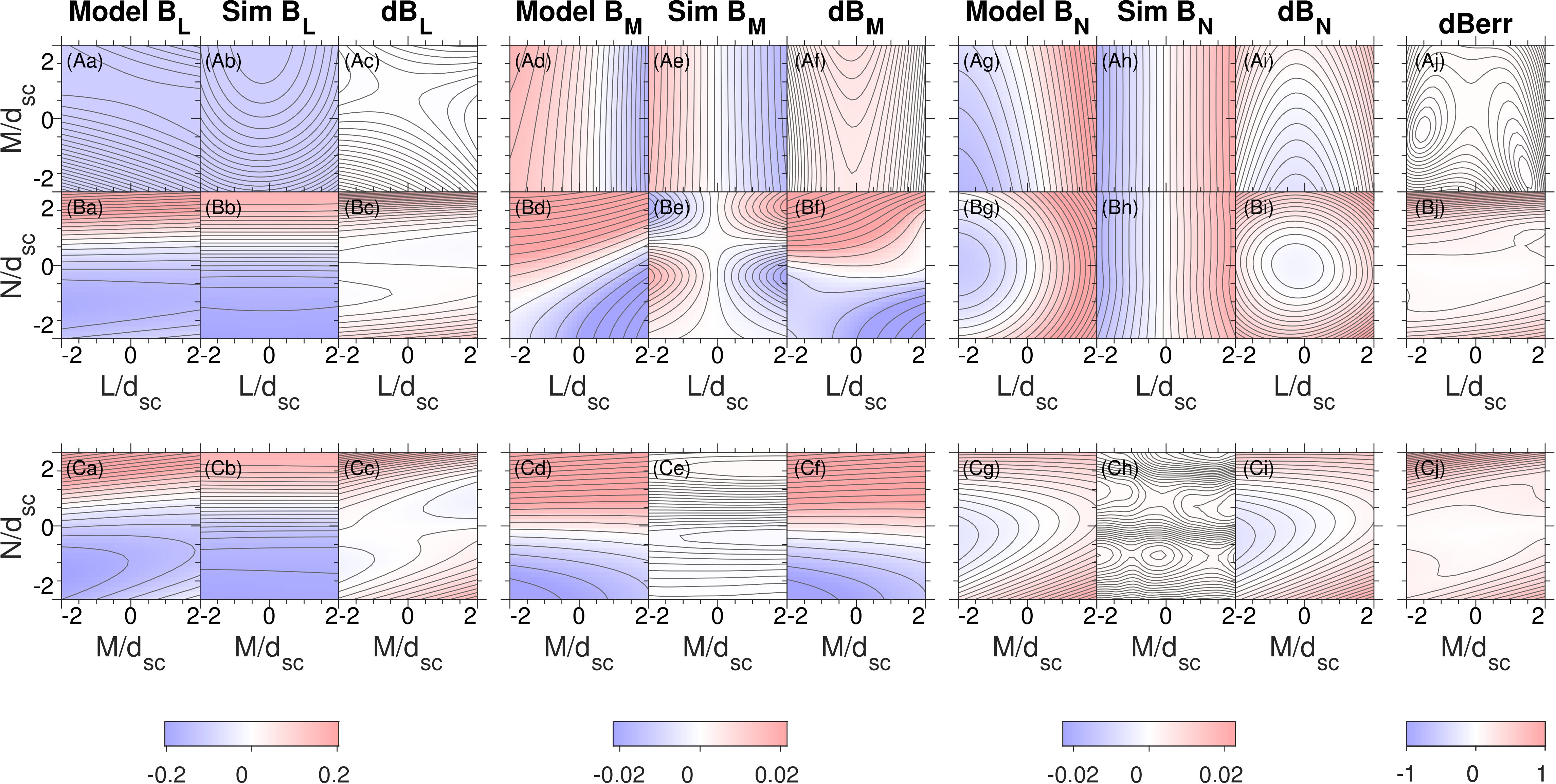

Model B_L
Sim B_L
dB_L
Model B_M
Sim B_M
dB_M
Model B_N
Sim B_N
dB_N
dBerr
(Aa)
(Ab)
(Ac)
(Ad)
(Ae)
(Af)
(Ag)
(Ah)
(Ai)
(Aj)
(Ba)
(Bb)
(Bc)
(Bd)
(Be)
(Bf)
(Bg)
(Bh)
(Bi)
(Bj)
(Ca)
(Cb)
(Cc)
(Cd)
(Ce)
(Cf)
(Cg)
(Ch)
(Ci)
(Cj)
M/d_{sc}
N/d_{sc}
L/d_{sc}
-2
0
2
-0.2
0.2
-0.02
0.02
-1
1

Figure 9.

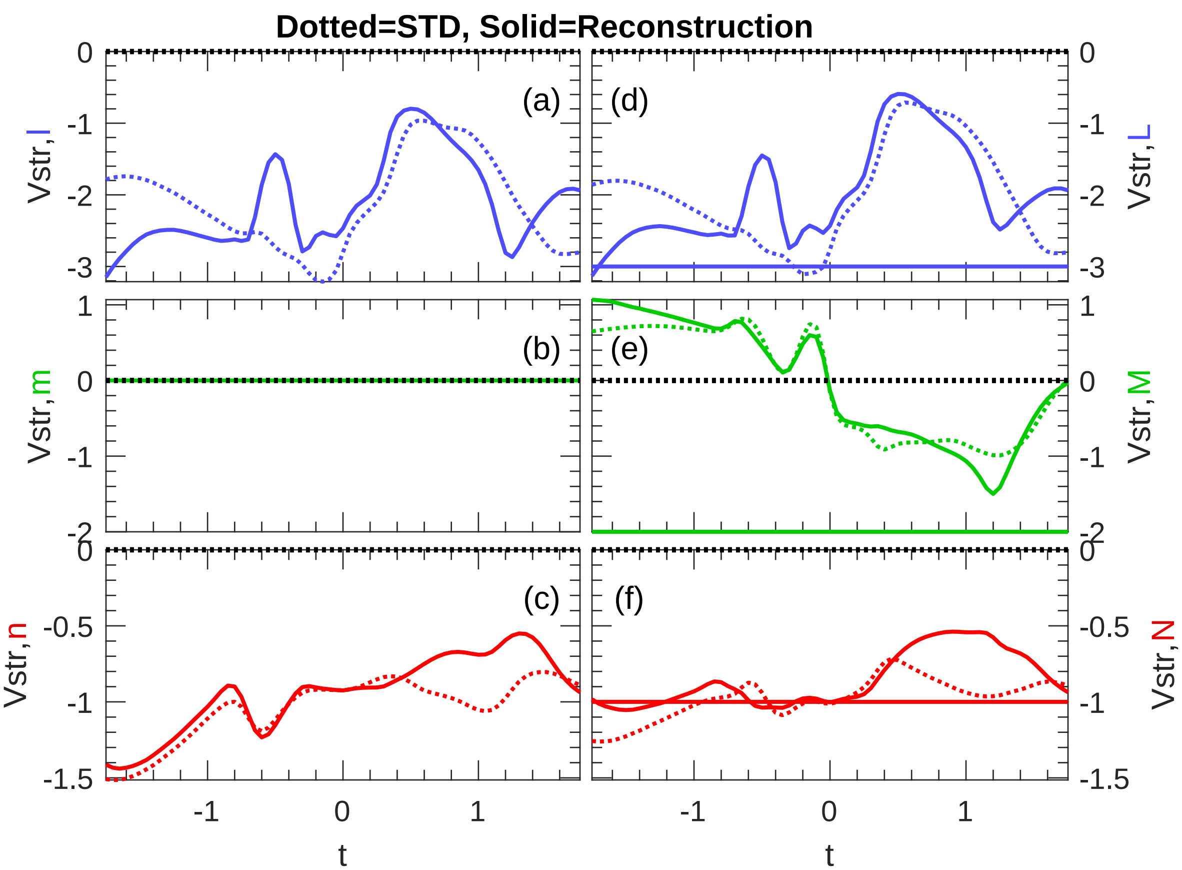

Dotted=STD, Solid=Reconstruction
(a)
(b)
(c)
(d)
(e)
(f)
Vstr, l
Vstr, m
Vstr, n
Vstr, L
Vstr, M
Vstr, N
0
-1
-2
-3
1
-0.5
-1.5
t

Figure 10.

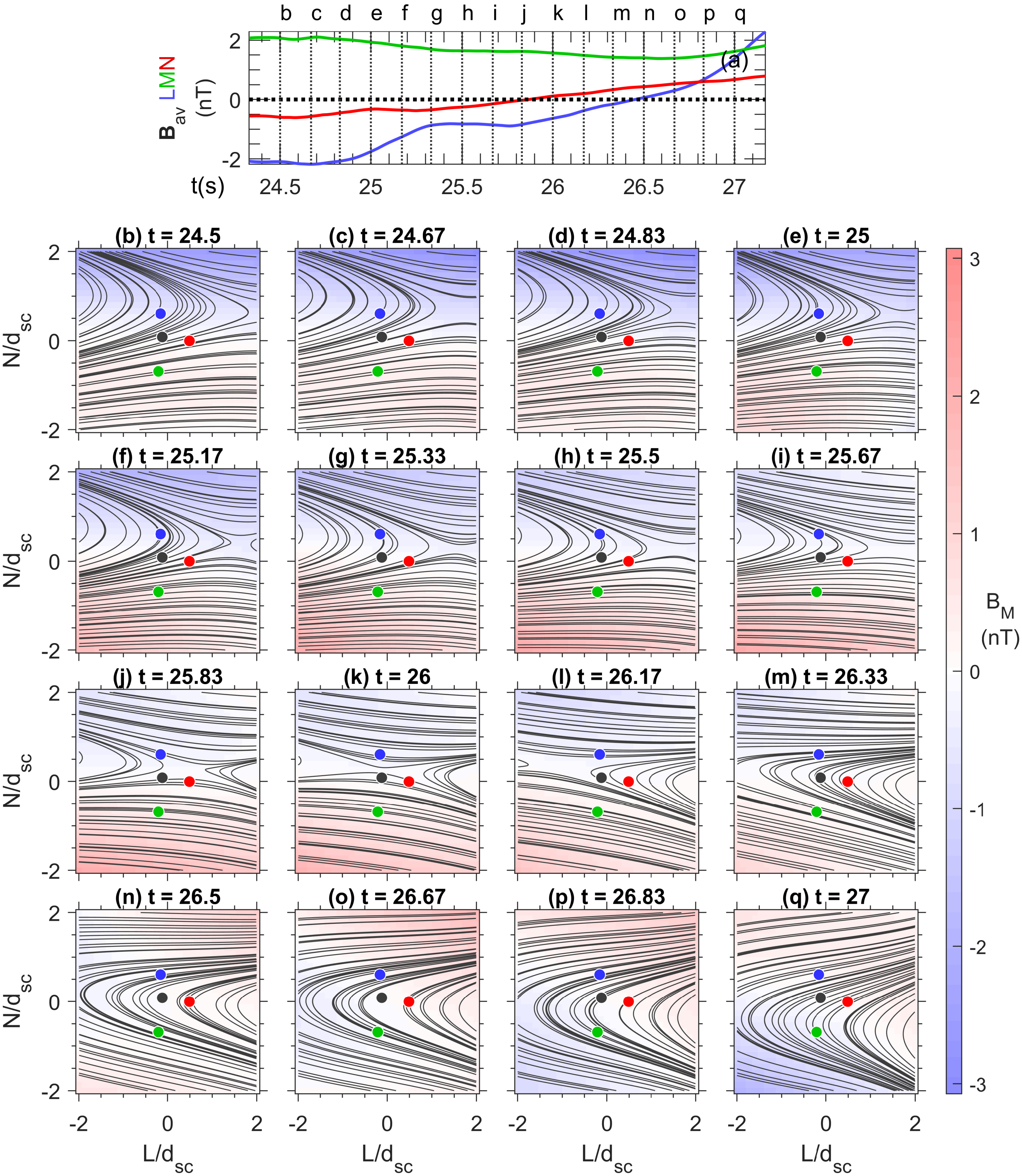

b c d e f g h i j k l m n o p q
(a)
B_{av} LMN (nT)
t(s)
24.5 25 25.5 26 26.5 27
(b) t = 24.5
(c) t = 24.67
(d) t = 24.83
(e) t = 25
(f) t = 25.17
(g) t = 25.33
(h) t = 25.5
(i) t = 25.67
(j) t = 25.83
(k) t = 26
(l) t = 26.17
(m) t = 26.33
(n) t = 26.5
(o) t = 26.67
(p) t = 26.83
(q) t = 27
N/d_{sc}
L/d_{sc}
B_M (nT)

Figure 11.

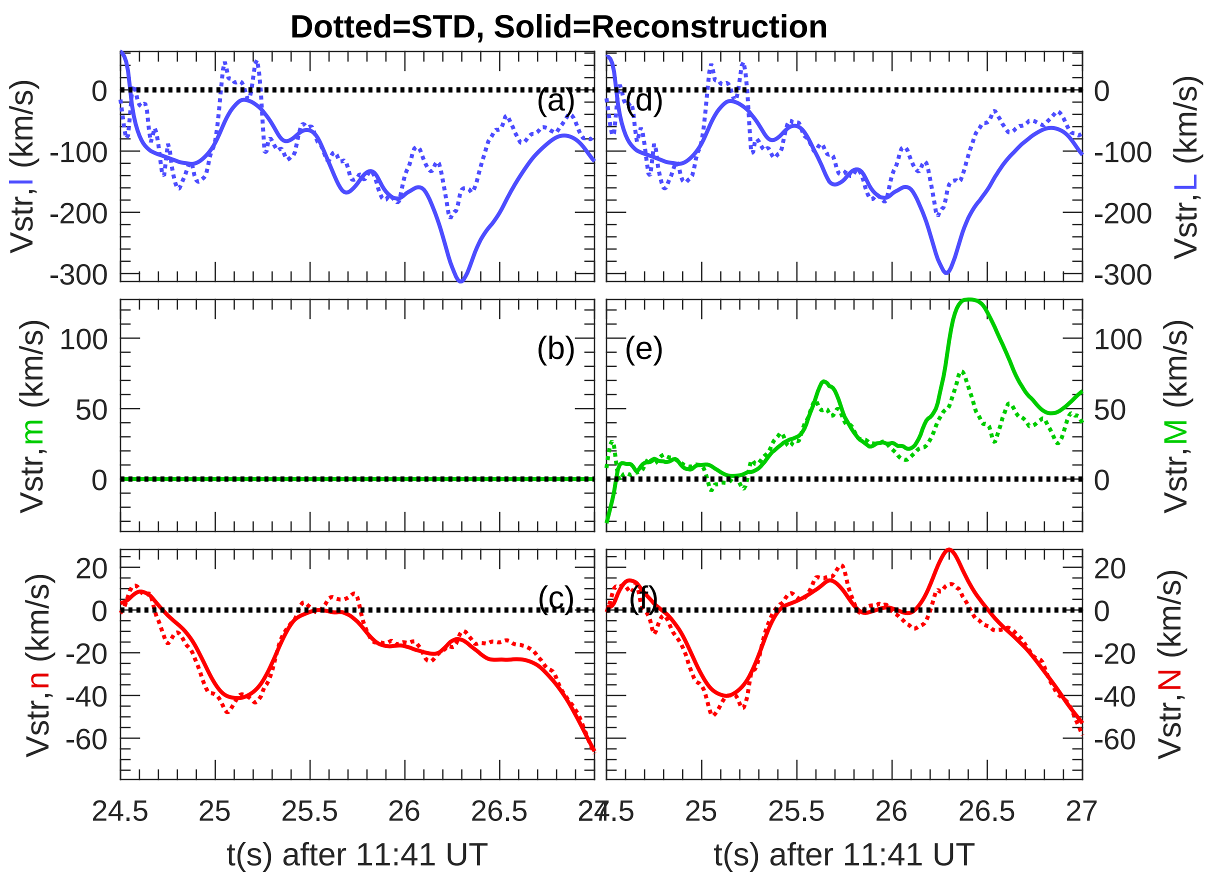

Dotted=STD, Solid=Reconstruction
(a)
(b)
(c)
(d)
(e)
(f)
Vstr, l (km/s)
Vstr, m (km/s)
Vstr, n (km/s)
Vstr, L (km/s)
Vstr, M (km/s)
Vstr, N (km/s)
0
-100
-200
-300
100
50
0
20
0
-20
-40
-60
24.5
25
25.5
26
26.5
27
t(s) after 11:41 UT
t(s) after 11:41 UT

Figure 12.

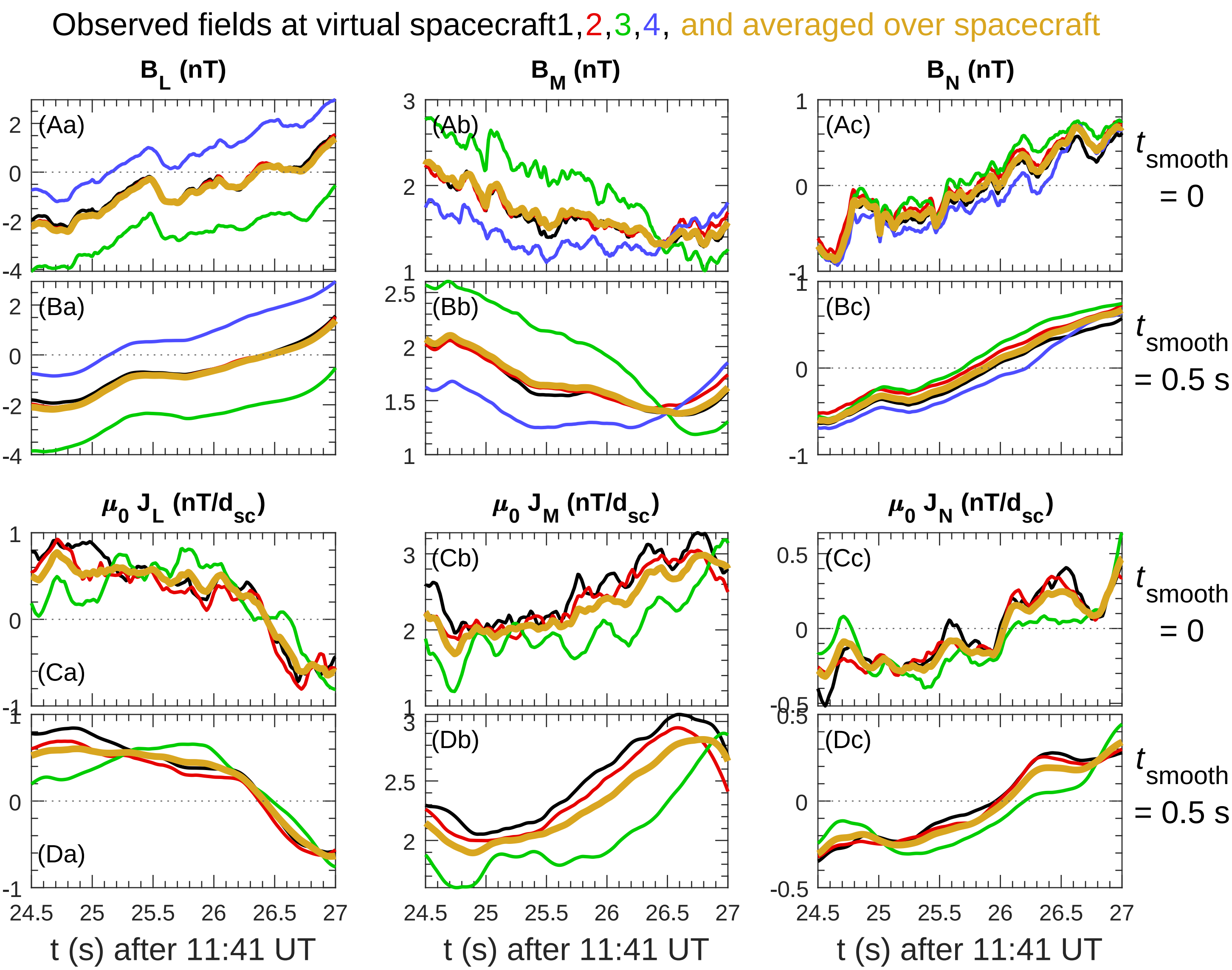

Observed fields at virtual spacecraft1,2,3,4, and averaged over spacecraft
B_L (nT)
B_M (nT)
B_N (nT)
(Aa)
(Ab)
(Ac)
(Ba)
(Bb)
(Bc)
μ0 J_L (nT/d_sc)
μ0 J_M (nT/d_sc)
μ0 J_N (nT/d_sc)
(Ca)
(Cb)
(Cc)
(Da)
(Db)
(Dc)
t_smooth = 0
t_smooth = 0.5 s
t_smooth = 0
t_smooth = 0.5 s
t (s) after 11:41 UT
t (s) after 11:41 UT
t (s) after 11:41 UT

Figure 13.

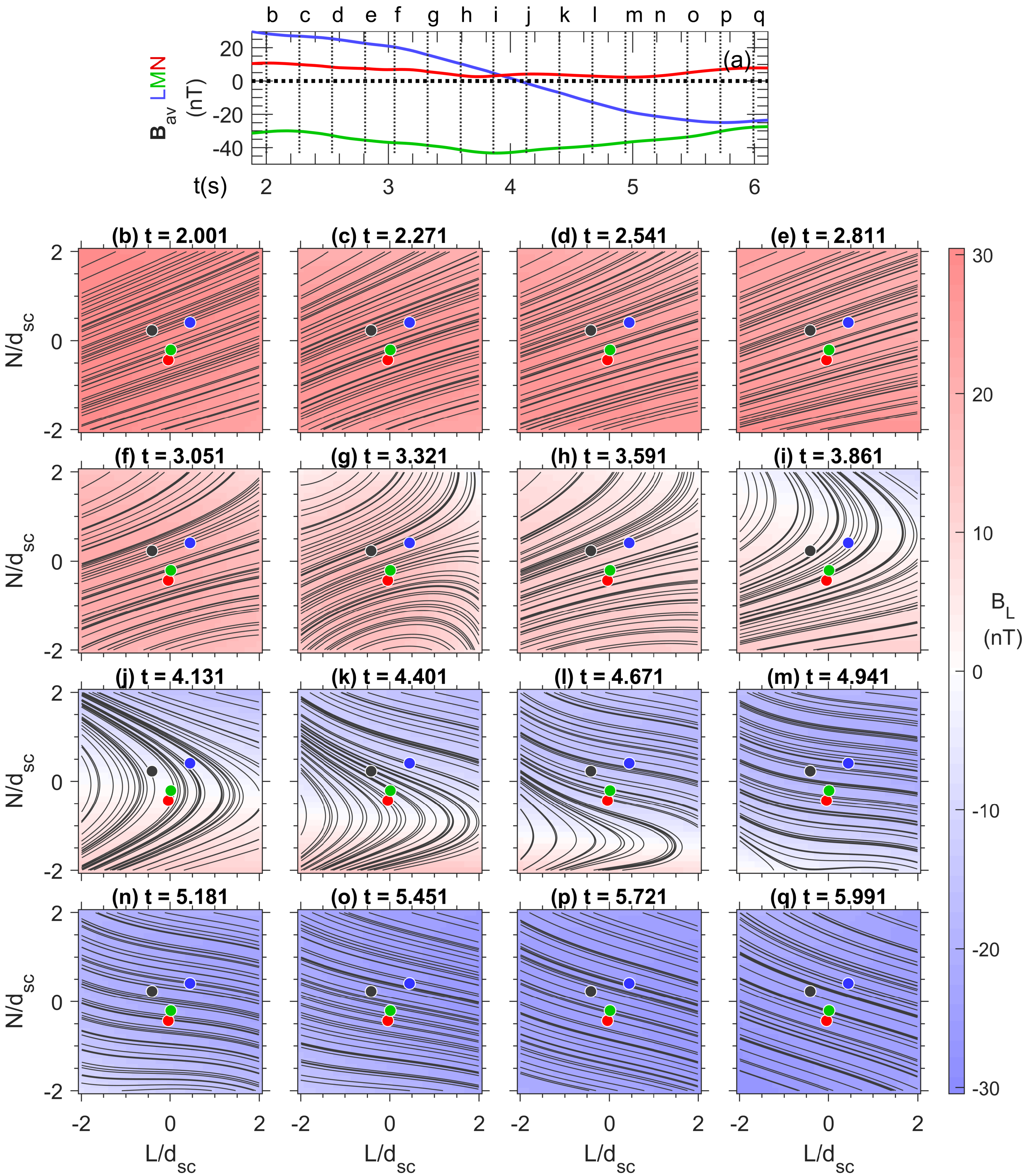

b c d e f g h i j k l m n o p q
B_{av} LMN (nT)
(a)
t(s)
(b) t = 2.001
(c) t = 2.271
(d) t = 2.541
(e) t = 2.811
(f) t = 3.051
(g) t = 3.321
(h) t = 3.591
(i) t = 3.861
(j) t = 4.131
(k) t = 4.401
(l) t = 4.671
(m) t = 4.941
(n) t = 5.181
(o) t = 5.451
(p) t = 5.721
(q) t = 5.991
N/d_{sc}
L/d_{sc}
B_L (nT)

Figure 14.

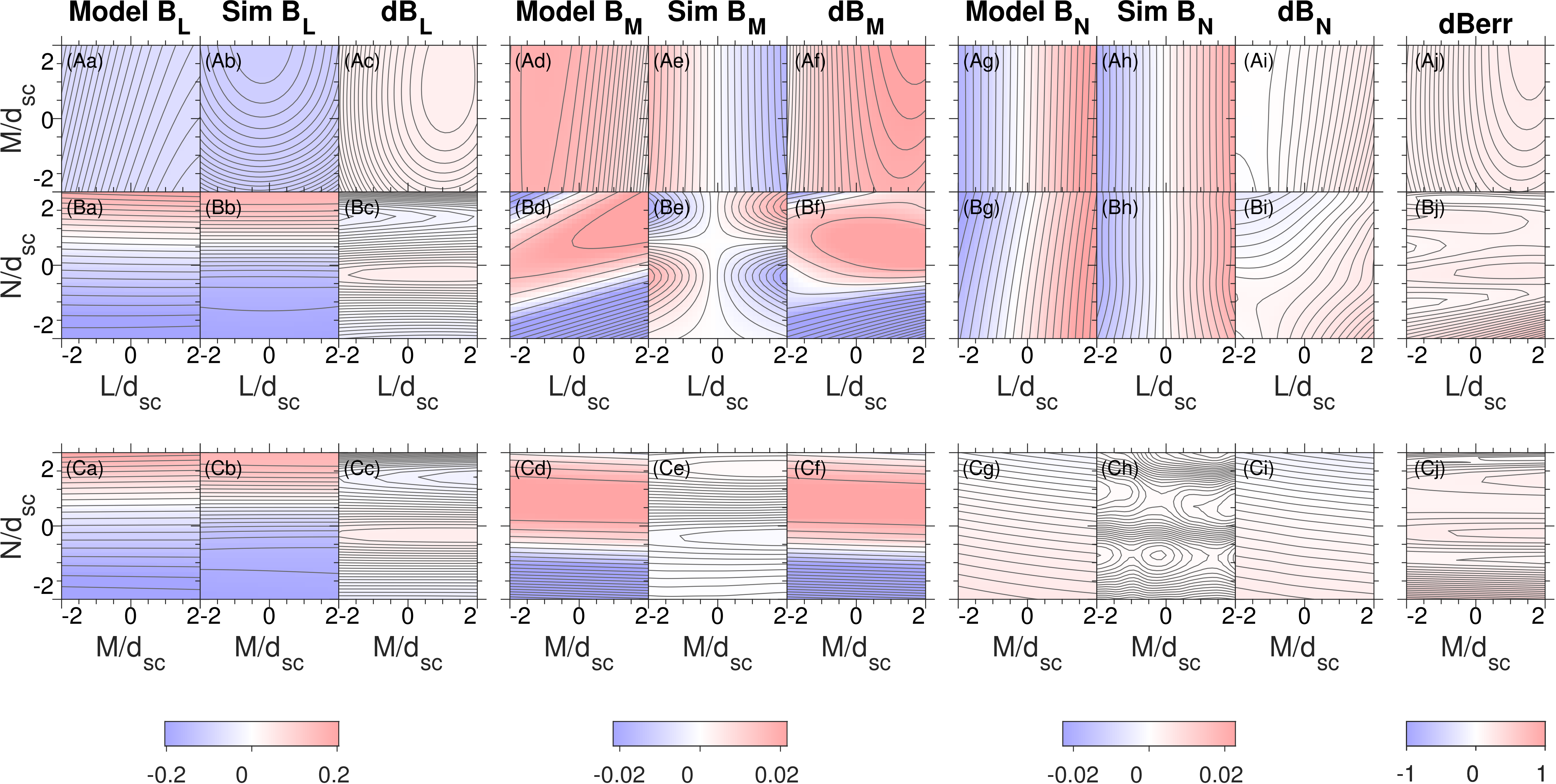

Model B_L
Sim B_L
dB_L
Model B_M
Sim B_M
dB_M
Model B_N
Sim B_N
dB_N
dBerr
(Aa) (Ab) (Ac) (Ad) (Ae) (Af) (Ag) (Ah) (Ai) (Aj)
(Ba) (Bb) (Bc) (Bd) (Be) (Bf) (Bg) (Bh) (Bi) (Bj)
(Ca) (Cb) (Cc) (Cd) (Ce) (Cf) (Cg) (Ch) (Ci) (Cj)
M/d_{sc}
N/d_{sc}
L/d_{sc}
-0.2 0 0.2
-0.02 0 0.02
-0.02 0 0.02
-1 0 1